Competitive adsorption geometries for the arsenate As(V) and phosphate P(V) oxyanions on magnetite surfaces: Experiments and theory

XIAOLIANG LIANG [1, 6, 7], XIAOJU LIN [1, 7], GAOLING WEI [2, 3], LINGYA MA [1, 6, 7], HONGPING HE [1, 6, 7 *], DAVID SANTOS-CARBALLAL [4 *], JIANXI ZHU [1, 6, 7], RUNLIANG ZHU [1, 6, 7], NORA H. DE LEEUW [4, 5]

[1] CAS Key Laboratory of Mineralogy and Metallogeny/Guangdong Provincial Key Laboratory of Mineral Physics and Material Research & Development, Guangzhou Institute of Geochemistry, Chinese Academy of Sciences, Guangzhou 510640, PR China;

[2] Guangdong Key Laboratory of Integrated Agro-environmental Pollution Control and Management, Guangdong Institute of Eco-environmental Science & Technology, Guangzhou 510650, China;

[3] National-Regional Joint Engineering Research Center for Soil Pollution Control and Remediation in South China, Guangzhou 510650, China;

[4] School of Chemistry, University of Leeds, Leeds LS2 9JT, United Kingdom;

[5] Department of Earth Sciences, Utrecht University, Princetonplein 8A, 3584 CD Utrecht, The Netherlands;

[6] Institutions of Earth Science, University of Chinese Academy of Sciences, Beijing 100049, P.R. China;

[7] University of Chinese Academy of Sciences, Beijing 100049, PR China.

*Corresponding author. E-mail: hehp@gig.ac.cn (H.P. HE);

D.Santos-Carballal@leeds.ac.uk (D. Santos-Carballal).

ABSTRACT

In the present study, the competitive adsorption geometries for arsenate and phosphate on magnetite surfaces over a pH range of 4-9 was investigated using *in situ* attenuated total reflectance Fourier-transform infrared spectroscopy (ATR-FTIR) and two-dimensional correlation analysis (2D-COS). The adsorption energies and infrared vibrational frequencies of these surface complexes were also calculated by first principles simulations. Arsenate and phosphate have different preferences for the magnetite surface in the presence of aqueous solvent at both acid and alkaline pH. For the adsorption of phosphate, mono-protonated monodentate mononuclear (MMM) complexes dominated at acid pH, while non-protonated bidentate binuclear (NBB) complexes were dominant at alkaline pH. Arsenate mainly formed bidentate binuclear (BB) complexes with some outer-sphere species, both of which were more prevalent at acid pH. The pre-absorbed inner-sphere arsenate species were scarcely affected by the introduction of phosphate. However, the pre-absorbed phosphate oxyanions, especially the MMM complexes, were significantly substituted by BB arsenate at the magnetite surfaces. The adsorption affinity of phosphate and arsenate species for magnetite surface was found to increase in the following order: MMM phosphate complex < NBB phosphate complex < BB arsenate complex, which was consistent with the calculated adsorption energies. The simulated infrared vibrational frequencies for the most favored adsorption modes of each oxyanion display distinctive patterns, in which trends are in excellent agreement with experimental data.

The effects of pH, adsorption sequence and mineral species on the competitive adsorption between arsenate and phosphate oxyanions are also discussed, and their different competing ability and stability on the magnetite surfaces were ascribed to the variations in adsorption geometry and strength of binding. To the best of our knowledge, this is the first study aiming to distinguish the stability of the different phosphate and arsenate complexes on magnetite by employing a highly suitable combination of powerful *in situ* spectroscopy and DFT simulations.

This study provides molecular-level insight into the geometries and relative stabilities of the adsorption of phosphate and arsenate on magnetite surfaces, which is useful for the interpretation of the mobility and bioavailability of these anions.

Keywords: Phosphate; Arsenate; Competitive adsorption; Adsorption geometry; ATR-FTIR; First-principles simulations

INTRODUCTION

Contamination of soil and aquatic systems by arsenic (As) and phosphorus (P) is of global environmental concern. Arsenic is often found at elevated concentrations in freshwater, attributed to a variety of natural (e.g., geothermal processes and mineral weathering) and anthropogenic (e.g., mining industry and agriculture) processes (Kocourkova-Vikova et al., 2015; Kunhikrishnan et al., 2017). Owing to its biotoxicity and carcinogenic risk, the presence of arsenic in drinking water ranks among the greatest threat to public health (Antelo et al., 2015), which has led the World Health Organization to propose a limit of 10 μg L^{-1} (WHO, 2011). However, in ~~the~~ arsenic contaminated water, the As concentration can reach several ppm (Chakraborti et al., 2002; Sprague and Vermaire, 2018; Winkel et al., 2011). Arsenic exists in several oxidation states (-III, 0, III and V), with arsenate (AsO_4^{3-}) being the most common form found in natural aqueous systems (Choppala et al., 2016). Phosphorous (P) is an essential nutrient for plant growth. But the input of excess P from agricultural land runoff or over-fertilization may lead to levels above the limit of 0.1 mg L^{-1} recommended by the United States Environmental Protection Agency (USEPA), causing severe environmental problems including eutrophication (Neupane et al., 2014). P occurs naturally only in the pentavalent state, forming ortho-phosphates, pyrophosphates, longer-chain polyphosphates and several types of organic phosphates (Correll, 1998).

After their release from natural and anthropogenic sources, As and P undergo a series of geochemical reactions, e.g., adsorption, reduction/oxidation, precipitation (Zhang

et al., 2017b), and sequestration by soil and sediments (Grossl et al., 1997). The adsorption in the mineral/water interface is vital for their mobility. Iron (hydr)oxides are ubiquitous in soils and aquatic sediments (Pedersen et al., 2005), with high adsorption affinity towards arsenate and phosphate. The surface complexation is the dominant adsorption mechanism reported for arsenate and phosphate species, as verified in macroscopic batch experiments (Swedlund et al., 2014), model calculations (Tiberg et al., 2013) and microscopic studies (Johnston and Chrysochoou, 2014). Bidentate-binuclear (BB), monodentate-mononuclear (MM) and bidentate-mononuclear (BM) complexes are the prevalent surface binding configurations of arsenate and phosphate on iron oxides (Fendorf et al., 1997; Liu et al., 2015), with distribution dependent on pH, ionic strength, and surface coverage (Krumina et al., 2016). Generally, the ability to form bridging bidentate surface complexes is dependent upon the proximity of terminal Fe-O sites on the surface (Livi et al., 2017; Villalobos et al., 2009).

P and As belong to group 5A of the periodic table and form species with comparable chemical properties. Both arsenate and phosphate oxyanions have a tetrahedral geometry with close thermochemical radii, i.e., 2.48 and 2.38 Å (Silva and Fraustoda, 2001), respectively, and very similar proton affinities, e.g., 2.2, 7.0 and 11.5 for pKa$_1$, pKa$_2$ and pKa$_3$ of arsenate and 2.2, 7.2 and 12.3 for pKa$_1$, pKa$_2$ and pKa$_3$ of phosphate (Elzinga and Sparks, 2007; Mohan and Pittman, 2007). Thus, they display analogous adsorption characteristics in the aspects of kinetics, pH dependence, and effect of ionic strength. As arsenate and phosphate oxyanions frequently occur together in

surface environments, their competitive adsorption onto mineral surfaces explicitly determines their bioavailability and leachability, which is crucial for the prediction of potential risk of environmental contamination. However, the current knowledge on this hypothesis is scattered and fragmented, even regarding the adverse effect of phosphate on arsenate adsorption. For example, arsenate is found preferentially adsorbed on iron oxide at a low pH, whereas phosphate shows the opposite trend (Han and Ro, 2018). But in soil stabilized by iron oxide, phosphate can replace the adsorbed arsenate when the concentration of the former is larger than the latter (So et al., 2012). This is contrary to the results reported by Hashem et al., where arsenate was found bonded to iron oxide more strongly than phosphate (Hashem et al., 2015). Moreover, contradictory information is also found in the literature concerning the adsorption geometry. For arsenate, BB complexes were considered ~~as~~ the predominant adsorption configuration on iron oxide surfaces (Carabante et al., 2010). MM coordination is also found for arsenate binding on some iron oxides, as verified by combined EXAFS and IR analyses (Antelo et al., 2015; Loring et al., 2009). Although BM configuration has also been assigned under certain conditions (Neupane et al., 2014), these have been excluded by Sherman et al., as the EXAFS signal attributed to the BM complex was simply due to multiple scattering (Sherman and Randall, 2003). For phosphate, the IR analysis indicates that protonated BB complexes are the predominant species on iron oxides at pH between 3 and 6, whereas the non-protonated BB complexes are dominant at pH > 7.5 (Carabante et al., 2010). On the contrary, ~~the~~ surface complexation modeling (SCM) predicts that deprotonated BB

122 phosphate and deprotonated MM phosphate dominate at lower pH and higher pH
123 values, respectively, while the contribution of protonated BB is very small
124 (Kanematsu et al., 2010). This shows ~~that~~ great divergence in the competitiveness
125 ~~exists~~ not only within the individual adsorption geometries of phosphate and arsenate,
126 but also during their co-adsorption.
127 To date, the competitive adsorption of arsenate and phosphate on calcite (So et al.,
128 2012), clay minerals (Violante and Pigna, 2002), and certain iron oxides, e.g.,
129 ferrihydrite (Antelo et al., 2015) and goethite (Zhao and Stanforth, 2001), has been
130 investigated intensively. In comparison, their competitive adsorption on magnetite,
131 which is a common constituent of soil and sediment, is poorly understood. Magnetite
132 exists in anoxic sediments and soils (Guo and Barnard, 2013), and is formed naturally
133 via several pathways, including ferrous iron oxidation and iron metal corrosion, as
134 well as chemical and biological reduction of ferric oxides (Gorski et al., 2010).
135 Additionally, the remediation of contaminated groundwater and soil is increasingly
136 carried out using an emerging technology based on zero-valent iron (ZVI)
137 nanoparticles, where magnetite is the major corrosion product formed as the outer
138 layer of ZVI (Filip et al., 2014). With the inverse spinel structure, magnetite has
139 several features that make its reaction properties interesting; specifically, (i) electron
140 donor Fe^{2+} ions on octahedral sites, which are active for the reduction of certain
141 oxyanions, e.g., CrO_4^{2-} and UO_3^-; and (ii) octahedral Fe^{2+} and Fe^{3+} cations which can
142 oxidize and reduce reversibly during the reaction with adsorbed oxyanions, while
143 keeping the spinel structure unaffected. In previous studies, magnetite is shown to be

144 efficient at scavenging metal oxyanions in natural and engineered aquatic systems,
145 including chromate (Zhang et al., 2017a), arsenate (Zhang et al., 2011), and uranyl
146 (Scott et al., 2005). These properties and behavior highlight the important role of
147 magnetite in the transport of arsenate and phosphate in soil and aqueous systems. Due
148 to the low specific surface area or surface site density of magnetite (<50 m^2 g^{-1}, 1–2
149 sites nm^{-2}) (Sun et al., 1998; Tamura et al., 1993), relative to ferrihydrite (>200 m^2 g^{-1},
150 2.5–3 sites nm^{-2}) (Hiemstra, 2013) and goethite (<50 m^2 g^{-1}, 2.5–3.5 sites nm^{-2})
151 (Ona-Nguema et al., 2005; Zhao and Stanforth, 2001), the resulting low surface
152 coverage of arsenate and phosphate on magnetite makes it difficult to analyze
153 spectroscopically. Extended X-ray absorption fine structure (EXAFS) spectroscopy is
154 the most widespread technique used to investigate the geometry of surface complexes
155 (Ona-Nguema et al., 2005), which has shown the formation of BB arsenate complexes
156 on the surfaces of ferrihydrite, hematite, goethite and lepidocrocite (Sherman and
157 Randall, 2003). However, it is difficult to analyze light elements such as P using soft
158 X-rays, due to their poor signal-to-noise ratios. *In situ* attenuated total reflectance
159 Fourier-transform infrared (ATR-FTIR) spectroscopy is a reliable method that is
160 capable of tracing the coordination environment and protonation state of most
161 oxyanions at mineral-water interfaces without interference of signals from the liquid
162 phase (Brechbuhl et al., 2012). Although the in individual and competitive
163 coordination structure of phosphate and arsenate on ferrihydrite, geothite and hematite
164 has been previously investigated using ATR-FTIR, the analysis of the relatively broad
165 vibrational bands led to inconclusive interpretation (Gao et al., 2013). Recently,

two-dimensional correlation spectroscopy (2D-COS) has been successfully applied in ATR-FTIR analysis by resolving overlapped peaks and enhancing the spectral resolution (Yan et al., 2016). Despite the advances achieved using ATR-FTIR in the understanding of the adsorption mechanism and geometries of phosphate and arsenate complexes, it is still unclear what are the factors that drive their competition under complex and realistic conditions. This uncertainty may be resolved by employing periodic density functional theory (DFT) calculations and comparing the simulated geometries, vibrational modes, and/or relative adsorption energies to experimental results, which will provide a better understanding from a thermodynamic point of view of the competition between arsenate and phosphate (He et al., 2009).

In this study, the competitive adsorption of arsenate and phosphate species on the surface of chromium-doped magnetite was investigated by *in situ* ATR-FTIR spectroscopy and complemented by DFT calculations. An interesting feature of natural magnetite is the substitution of iron by other metals, while maintaining the spinel structure. Cr is the a common impurity element in natural magnetite as trace element (less than 0.1%), minor element (0.1%-1%) and major element (more than 1%), forming solid solution series between magnetite (Fe_3O_4) and chromite ($FeCr_2O_4$) (Dupuis and Beaudoin, 2011). Moreover, the substitution of Cr^{3+} for Fe^{3+} is known to enhance the adsorption capacity of magnetite (Liang et al., 2012), and thus increase the signals and accuracy of *in situ* ATR-FTIR experiments. The competitive adsorption was carried out under different addition subsequences. A discussion and comparison between our results and previous investigations was also conducted and a

188 comprehensive atomic-level understanding on the adsorption of phosphate and
189 arsenate on magnetite is used to better interpret their geochemical behaviors in the
190 earth surface and their effects on nucleation, growth, and phase transformation of the
191 mineral phases.
192
193 **MATERIALS AND METHODS**
194 **Preparation of Cr-substituted magnetite**
195 Magnetite with Cr substitution was synthesized by the precipitation-oxidation method
196 described in Text A.1. The obtained sample had the spinel structure (Figure. A.1) and
197 X-ray absorption fine structure (XAFS) spectra illustrated that chromium in the
198 valence state of +3 mainly occupies the octahedral sites. The detailed discussion of
199 XAFS results has been presented elsewhere (Liang et al., 2013). The high surface area
200 (112 m^2 g^{-1}) and surface site density (3.6 sites nm^{-2}) of the magnetite particles (Table
201 A.1) increased the likelihood of obtaining good contact and allowed us to probe large
202 quantities of adsorbed species (Liang et al., 2017). During the adsorption, the
203 concentration of leaching Cr and Fe was below the detection limit of the instrument.
204
205 **In situ ATR-FTIR and 2D-COS analyses**
206 *In situ* ATR-FTIR analysis of phosphate and arsenate adsorption on magnetite was
207 conducted using a Bruker Vertex 70 FTIR spectrometer equipped with a liquid
208 N_2-cooled MCT detector and a horizontal ATR accessory made of ZnSe crystal.
209 Before the IR analysis, the magnetite particle layer was prepared on the ZnSe crystal.

1 mL of magnetite suspension (5 g L^{-1}) was dropped onto the crystal surface and dried overnight at room temperature. The film was then rinsed with deionized (DI) water to remove the loosely deposited particles, which stabilized the deposited layer (Hug, 1997). At the end of adsorption experiment, the magnetite film was inspected for signs of film erosion, which were not observed.

Before adsorption, a NaCl background electrolyte solution (0.01 mol L^{-1}) at the designated pH was flowed through the cell with magnetite deposition layer at a rate of 1 mL min^{-1} until no further change in spectra was seen. A background spectrum comprising the absorbance of the ZnSe crystal and the deposited adsorbent was then collected, followed by the injection of solutions containing 100 μmol L^{-1} of arsenate or phosphate, and 0.01 mol L^{-1} of NaCl to start the adsorption reaction. IR spectra were recorded as a function of time until the adsorption reached equilibrium without any signal variation. NaCl was selected as the background electrolyte, because it was inert or non-adsorbed on solid surfaces. All liquid samples were purged with N_2 during spectrum collection. The pH was adjusted within the range of 4.0–9.0 using NaOH (0.1 mol L^{-1}) and HCl (0.1 mol L^{-1}). Desorption experiments were conducted by introducing NaCl solution (0.01 mol L^{-1}) into the ZnSe cell when the adsorption of oxyanions reached equilibrium. The comparative adsorption was carried out through the reversible substitution of arsenate solution (100 μmol L^{-1} at pH 4.0 and 7.0, and 500μmol L^{-1} at pH 9.0) with phosphate solution of the same concentration. It is necessary to emphasize that the arsenate concentrations used in this study, i.e., 100 and 500 ppm are at the low end of the range of concentrations examined in past

232 experimental studies (molecular-scale studies: 5 to 10000 μmol L^{-1}, macroscopic
233 studies: 0.7 to 30000 μmol L^{-1}), as indicated by Catalano, et al. (Catalano et al., 2008).
234 The IR spectra were processed and analyzed with the OPUS software. Curve-fitting
235 analysis of the peaks was conducted using the Gaussian line shape. To obtain an
236 accurate assignment of the IR peaks for the surface complexes, the spectra were
237 analyzed using the 2D-COS technique (Text A.2).
238
239 **Computational methods**
240 To simulate the interaction between the Fe_3O_4(001) surface and phosphate/arsenate
241 oxyanions in aqueous solution, the periodic plane-wave density functional theory
242 (DFT) method within the Vienna *ab-initio* simulation package (VASP) was employed
243 (Kresse and Furthmuller, 1996a; Kresse and Furthmuller, 1996b; Kresse and Hafner,
244 1993; Kresse and Hafner, 1994). The Perdew, Burke and Ernzerhof (PBE) semi-local
245 functional approximation was used to calculate the exchange-correlation energy
246 (Perdew et al., 1996; Perdew et al., 1997). The projector augmented wave (PAW)
247 method was used to model the atomic frozen core states and their interaction with the
248 valence levels (Fe: 4*d*5*s*, O: 2*s*2*p*, H: 1*s*, P: 3*s*3*p* and As: 4*s*4*p*) (Blochl, 1994; Kresse
249 and Joubert, 1999). The expansion of the Kohn-Sham (KS) valence states was
250 calculated with a kinetic energy cut-off of 400 eV. We have tested larger cut-off values,
251 but these led to negligible energy differences with respect to a reference, such as the
252 adsorption energies reported in our previous studies (Santos-Carballal et al., 2018;
253 Santos-Carballal et al., 2014). The electronic partial occupancies were determined

during geometry optimizations using the Gaussian smearing method with the width set at 0.02 eV (Mermin, 1965). Furthermore, the tetrahedron method with Blöchl corrections was used in static simulations to obtain accurate total energies as well as all the electronic and magnetic properties. Long-range dispersion interactions were modeled using the D2 semi-empirical method of Grimme (Grimme, 2006). The optimization of the structures was conducted *via* the conjugate-gradients method, which stopped when the forces on all atoms were smaller than 0.01 $eV \cdot Å^{-1}$. The Dudarev *et al.* (Dudarev et al., 1998) approach was used within the DFT+*U* methodology (Anisimov et al., 1992) to improve the description of the localized and strongly correlated Fe *d* states, which were corrected by applying the value of U_{eff} = 3.7 eV (Santos-Carballal et al., 2018; Santos-Carballal et al., 2014). All calculations were spin-polarised and the initial magnetic moments were set following a high-spin ferrimagnetic structure, *i.e.* with opposite spins in the tetrahedral and octahedral sites (Neel, 1948; Shull et al., 1951). These criteria allowed convergence of the total electronic energy within 10^{-4} eV per atom. We decided to only model the magnetite (001) surface as this is the thermodynamically most stable facet, with the lowest relaxed surface energy and the most prominent plane in the calculated crystal morphology (Santos-Carballal et al., 2014), which is in agreement with the observations made by Zhao *et al.* at pH ≤ 13 (Zhao et al., 2008). Moreover, Jönsson and Sherman found that the bidentate interaction of the inner-sphere As(V) complexes is only possible at the rows of exposed Fe_B ions formed in the [011] direction of the magnetite (001) surface (Jonsson and Sherman, 2008), which is in line with its largest

density of exposed Fe cations (Santos-Carballal et al., 2014). However, similar to goethite, we cannot rule out that that arsenate and phosphate may have different affinities for other less stable and less prominent magnetite surfaces, which may saturate with a small fraction of the total number of adsorbed oxyanions (Kubicki et al., 2012), thus providing a minor contribution to the observed infrared spectra. For the inner-sphere complexes, the adsorption of the phosphate and arsenate species on the $Fe_3O_4(001)$ surface was simulated under both acid and alkaline conditions. Different initial binding geometries, including MM, BM, BB and tridentate trinuclear (TT), were taken into account. All possible binding sites were also inspected, including the protruding Fe_A atom and the Fe_B ion as well as their possible combinations. Thus, we are confident that we have considered all possible adsorption geometries for the oxyanion complexes. However, given the large positional degree of freedom of the water molecules, there may be some uncertainty in their location, but this lies beyond the scope of this work. Further details of the computational methods used, including surface models, inner- and outer-sphere complex models, approach used for the simulation of acid and alkaline conditions, calculation of adsorption energy, Bader charges and vibrational frequencies are presented in Text A.3 and Figure A.2.

295 ## RESULTS AND DISCUSSION

296 ### Individual molecular adsorption

297 Arsenate adsorption on magnetite

298 The intensity of characteristic bands obtained by *in situ* ATR-FTIR was
299 proportional to the level of adsorption; as pH decreased, the arsenate adsorption was
300 obviously enhanced (Figure A.3). Given the point of zero charge (PZC) of magnetite
301 at 6.8 (Table A.1), the surface of this mineral gradually changed from negative charge
302 at alkaline pH to positive charge under acid conditions, improving the adsorption of
303 arsenate oxyanions. Besides band intensity, the spectrum profile also showed
304 significant changes with pH. At high pH, the spectra displayed a broad but
305 asymmetrical band at 855 cm^{-1}, with a shoulder peak at 820 cm^{-1}. As the pH decreases,
306 the band at 855 cm^{-1} became more symmetrical and sharpened, which was also
307 characteristic of aqueous $HAsO_4^{2-}$ (Figure. A.4). Thus, outer-sphere (OS) $HAsO_4^{2-}$
308 complexes were formed on magnetite at acidic pH, which was verified in desorption
309 experiments at pH = 4.0 (Figure. A.5). Once the arsenate solution was replaced by
310 NaCl solution, the intensity of the band at 855 cm^{-1} quickly decreased in 10 min, and
311 then slowly declined in the following 140 min, suggesting the coexistence of both OS
312 and inner-sphere (IS) arsenate complexes, as OS species have faster desorption rates
313 than IS species (Catalano et al., 2008). According to previous work, neither As(III)
314 oxidation nor As(V) reduction occurs on the magnetite surface (Jonsson and Sherman,
315 2008).

316 According to the 2D-COS analysis results (Text A.5), the band at 855 cm^{-1} and those

317 at 870, 830 and 805 cm^{-1} are attributed to different adsorption complexes of arsenate.
318 The band at 855 cm^{-1} was identical to that of aqueous $HAsO_4^{2-}$ (Figure A.4),
319 supporting the formation of these OS complexes. The contribution at 870 cm^{-1} was
320 assigned to the asymmetric stretching (ν_3) of As-O, while those at 830 and 805 cm^{-1}
321 were assigned to the asymmetric and symmetric stretchings (ν_3) of As-OFe,
322 respectively (Brechbuhl et al., 2012; Hu et al., 2015). The presence of three ν_3 bands
323 indicated the C_{2v} or lower symmetry for the IS arsenate complexes. The above
324 characteristic bands are consistent with the observations of arsenate adsorption on
325 ferrihydrite, hematite and rutile (Brechbuhl et al., 2012; Hu et al., 2015). Gao et al.
326 attributed the IR bands at 830 and 804 cm^{-1} to the arsenate adsorbed in the BB
327 geometry on the ferrihydrite surfaces at high pH (Gao et al., 2013). The BB
328 complexes are also the dominant geometry of arsenate adsorbed on most iron
329 (hydr)oxides, as verified by EXAFS (Jonsson and Sherman, 2008; Sherman and
330 Randall, 2003). Thus, in this study, the IS arsenate complexes on magnetite were also
331 assigned to the BB geometry.
332 The ATR-FTIR spectra were deconvoluted to gain additional insight into the arsenate
333 adsorption geometries (Figure. 1a). The relative amounts of adsorbed OS and IS
334 species and their contributions to the total adsorption (based on the sub-spectral area)
335 varied with pH (Figure. 2a). At pH > 7, almost no OS complexes were formed,
336 ascribed to the electrostatic repulsive force between the arsenate oxyanions and the
337 negatively charged magnetite surface. The IS complexes with BB geometry are the
338 main species at high pH (Eq. (1)). As the pH decreased, the magnetite surface became

positively charged, leading to the rapid increase in both the adsorption and contribution of OS complexes (Eq. (2)). Once the OS complexes were formed, the Coulombic attraction between the magnetite surface and arsenate oxyanions further improved the formation of IS complexes with BB geometry by ligand exchange. These findings explain why the IS species dominate over the OS complexes throughout the studied pH range.

$$2{\equiv}FeOH + HAsO_4^{2-} \rightarrow ({\equiv}FeO)_2(AsO)OH + 2OH^- \quad (1)$$

$${\equiv}FeOH_2^+ + H_2AsO_4^- \rightarrow {\equiv}FeOH_2^{+\cdots}HAsO_4^{2-} + H^+ \quad (2)$$

Phosphate adsorption on magnetite

The adsorption of phosphate on magnetite was also affected by pH (Figure. A.7). When pH decreased from 9.0 to 4.0, the IR spectra increased in intensity, and displayed variations in shape. Specifically, a blue-shift of the highest peak from 1028 (pH = 9.0) to 1050 cm^{-1} (pH = 4.0) was seen, alongside the appearance of two shoulder peaks at 1000 and 1100 cm^{-1}. The IR spectra of the adsorbed phosphate were clearly different from the aqueous phosphate oxyanions at identical pH (Figure. A.8), suggesting the formation of IS complexes. This is also confirmed in the desorption experiment at pH = 4.0 (Figure. A.9), where the IR intensity only decreased slightly after desorption for 180 min.

Based on the 2D-COS analysis (Text A.5), the IR bands of phosphate at 1075, 1028 and 965 cm^{-1} and those at 1108, 1050, 1000 and 870 cm^{-1} were assigned to different IS complexes of phosphate. Both complexes had three ν_3 vibrations, indicating a C_{2v}

symmetry or lower. Through the deconvolution of the spectra (Figure. 1b) and the calculation of its sub-spectral area (Figure. 2b), the contribution of each predominant adsorbed phosphate complex was calculated at acid and alkaline pH (Figure. 2b). Based on the very close IR signals at high pH, a complex with similar coordination environment and protonation degree to 1075, 1028 and 965 cm^{-1} was reported for the adsorption of phosphate onto ferrihydrite (1070, 1025 and 940 cm^{-1}) (Arai and Sparks, 2001; Carabante et al., 2010). These complexes were in a non-protonated form, as confirmed through the comparison of spectra obtained in D_2O and H_2O medium (Arai and Sparks, 2001). Considering their C_{2v} or C_1 symmetry and the alkaline pH range of stability, these non-protonated species were affiliated to BB complexes (Eq. (3)) (Arai and Sparks, 2001; Kubicki et al., 2012), which were also reported in the adsorption of phosphate on goethite (1089, 1044 and 945 cm^{-1}) (Kubicki et al., 2012) and hematite (1085, 1035, and 966 cm^{-1}) (Elzinga and Sparks, 2007). The bands at 1075 and 1028 cm^{-1} were attributed to the stretching of the PO_2 bond, while the 965 cm^{-1} peak belonged to Fe-O-P bending.

$$2{\equiv}FeOH + HPO_4^{2-} \rightarrow (FeO)_2PO_2^- + H_2O + OH^- \quad (3)$$

The dominant complexes at acid pH were the protonated species. In previous studies, the characterization of their coordination environments and protonation degree were controversial (Arai and Sparks, 2001; Elzinga and Sparks, 2007; Luengo et al., 2006; Tejedortejedor and Anderson, 1990), as the formations of $(XO_3)PO$ and $(XO_2)PO_2$ (X=Fe or H) were suggested. Protonated $(XO_3)PO$ species, including monoprotonated BB complexes ($(\equiv FeO)_2(OH)PO$, MBB) and di-protonated MM complexes

383 (≡$FeO(OH)_2PO$, DMM), were reported for the adsorption on ferrihydrite (1124, 1035
384 and 998 cm^{-1}) (Carabante et al., 2010), goethite (1123, 1006 and 982 cm^{-1}) (Luengo et
385 al., 2006; Tejedortejedor and Anderson, 1990), and hematite (1120, 1010 and 970 cm^{-1})
386 (Elzinga and Sparks, 2007). The bands at high frequency (≥ 1120 cm^{-1}) were
387 attributed to the P=O stretching of the $(XO_3)PO$ species (Arai and Sparks, 2001;
388 Elzinga and Sparks, 2007). The adsorption geometry of protonated $(XO_2)PO_2$, i.e.,
389 monoprotonated MM (≡$(FeO)(OH)PO_2$), was identified on ferrihydrite (1100, 1028
390 and 920 cm^{-1}) (Arai and Sparks, 2001) and hematite (1115, 1006 and 970 cm^{-1})
391 (Elzinga and Sparks, 2007). For these complexes, bands at ~1100 and ~1115 cm^{-1}
392 were assigned to the PO_2 group since its frequencies were between $\upsilon_{P=O}$ (1120 cm^{-1})
393 and $\upsilon_{P\text{-}OFe}$ (1000 cm^{-1}) (Tejedortejedor and Anderson, 1990). In the present study, the
394 phosphate complexes (1108, 1050 and 1000 cm^{-1}) that predominated at acid pH were
395 monoprotonated MM complexes (MMM) (Eq. (4)), as the band with the highest
396 frequency (1108 cm^{-1}) was too low to be assigned to the P=O stretching. The bands at
397 1108 and 1050 cm^{-1} were attributed to the stretching of the PO_2 bond, while those at
398 1000 and 870 cm^{-1} belonged to the Fe-O-P and P-OH bending, respectively. The
399 formation of the $FeOPO_3$ (C_{3v}) complexes were excluded, as they have a molecular
400 symmetry higher than the lowest C_{2v} allowed.

401 $\equiv FeOH + H_2PO_4^- \rightarrow \equiv FeO(PO_2)OH^- + H_2O$ (4)

402

403 **Competitive molecular adsorption**

404 Substitution of phosphate by arsenate

405 At pH = 4, the MMM complexes are the dominant phosphate species followed by the
406 NBB complexes (Figure. 2b). When the phosphate solution was substituted by an
407 arsenate solution of equal molar concentration, the bands of phosphate (1200–870
408 cm^{-1}) immediately decreased in intensity, suggesting their desorption from the
409 magnetite surface (upper panel of Figure. 3a). Simultaneously, the bands assigned to
410 the adsorbed arsenate in the region of 900–800 cm^{-1} appeared and their intensity
411 increased with the adsorption time. This became more obvious upon subtracting the
412 equilibrium spectrum for the adsorbed arsenate recorded at 270 min, from the signals
413 recorded at 135 min, i.e., immediately before the introduction of arsenate. This
414 subtraction highlighted only the bands for which intensity decreased (positive bands)
415 or increased (negative bands) (lower panel of Figure. 3a). Based on the spectral
416 integration, 32% of adsorbed phosphate was replaced by arsenate. The proportion of
417 phosphate substituted by arsenate was close to the replacement found in previous
418 studies using ferrihydrite and goethite (O'Reilly et al., 2001). For example, Carabante
419 et al. reported that 35% of phosphate was desorbed from the ferrihydrite surface by
420 arsenate using D_2O as solvent at pD = 4 (Carabante et al., 2010), while Liu et al. and
421 Neupane et al. found that between 26%-28% of the absorbed phosphate on goethite
422 and ferrihydrite surfaces was replaced by arsenate (Liu et al., 2001; Neupane et al.,
423 2014). In order to determine the coordination environments, the positive bands in the
424 range 1200-870 cm^{-1} were deconvoluted into three contributions at 1108, 1050 and

1000 cm^{-1}, which were assigned to MMM phosphate complexes. Moreover, the negative bands at 870, 827 and 801 cm^{-1} were attributed to arsenate BB complexes (Figure. 3a).

Similar competitive experiments were also conducted under neutral (pH = 7, Figure. 3b) and alkaline conditions (pH = 9, Figure. 3c), where partial substitution of phosphate by arsenate was also observed. At pH = 7.0, the amount of phosphate adsorbed as MMM and NBB complexes were comparable (Figure. 2b). However, the integral spectrum of the NBB complexes (1075, 1026 and 960 cm^{-1}) was much lower than for the MMM complexes (1100, 1050, 1000cm^{-1}, Figure. 3b). The differences between the integrals of these bands indicates that the desorption of the MMM complexes was more significant than for the NBB, which was also found in the desorption of phosphate from ferrihydrite (Carabante et al., 2010).

To enhance the IR signal of the IS species at alkaline pH (Figure. 2), the concentrations of both phosphate and arsenate were increased from 100 μmol L^{-1} to 500 μmol L^{-1} (Figure. 3c). The desorption of phosphate (~15%) was lower under alkaline conditions than at acid pH (~32%) (Figure. 3a), where the removal of both MMM and NBB complexes was comparable. Based on the integral area of the difference spectrum, the proportion of desorbed NBB complexes was below 15% of the total adsorbed phosphate. Moreover, the NBB complexes required 350 min to achieve desorption equilibrium, which was much slower than the removal of MMM at acid and neutral pH (135 min).

447 Substitution of arsenate by phosphate

448 At pH = 4, the adsorbed arsenate was mainly forming BB complexes, with a low
449 proportion of OS species (Figure. 2a). After the introduction of phosphate solution of
450 equal molar concentration, the bands in the region of 1200–900 cm^{-1} corresponding to
451 phosphate appeared immediately and increased in intensity with time (Figure. 4a),
452 illustrating adsorption on magnetite surfaces. However, the IR intensity of arsenate
453 initially decreased slightly (~10%), but then stabilized, which suggests that the
454 phosphate oxyanions can only substitute partially the pre-adsorbed arsenate. After
455 subtracting the spectrum recorded just before the addition of phosphate and after its
456 adsorption had reached equilibrium, at 135 min and 270 min, respectively, the
457 positive bands related to adsorbed phosphate were located at 1108, 1050 and 1000
458 cm^{-1}. As mentioned above, these bands were associated with the MMM phosphate
459 complexes prevalent at acid pH. The negative bands that appeared at 852 and 798
460 cm^{-1} were attributed to the As-O asymmetrical stretching (υ_3) and the As-OH vibration
461 of the arsenate OS species (Hu et al., 2015).

462 Similarly to the competitive adsorption at pH = 4, phosphate could not substitute the
463 pre-adsorbed arsenate at neutral pH (Figure. 4b). The introduction of phosphate did
464 not lead to a decrease in the IR intensity of arsenate. Although the individually
465 absorbed phosphate species in neutral conditions were in equal proportions in both
466 MMM and NBB geometries (Figure. 2b), only the former configuration was stable
467 upon introduction of arsenate, as indicated by the phosphate bands at 1106, 1049, 994
468 and 896 cm^{-1}. Meanwhile, the difference spectrum did not show evidence of signals

from the desorbed arsenate, which confirms that the arsenate BB complexes are the dominant adsorption configuration, with a higher binding affinity than both the MMM and NBB phosphate complexes.

At alkaline pH, the amount of arsenate that adsorbed onto magnetite was low, resulting in a poor signal-to-noise ratio for the spectra. Thus, competitive adsorption under alkaline conditions was not analyzed in this study.

DFT calculations

Outer-sphere complexes

The outer-sphere (OS) complexes comprising the solute surrounded by water molecules are displayed in Figure. A.11. P-based anions are consistently smaller than their As-containing counterparts, as the intramolecular mean distance from the central atom to the oxygen ions differs by ~0.17 Å (Table 1). The degree of protonation of the solute does not noticeably affect the single and double bond distances (Table 1). As expected, the Bader charges of the solute ions are underestimated by ~17% with respect to their formal charges, which increases to ~23% with the pH value (Table 2). For the outer-sphere complexes under alkaline conditions, a charge of approximately $-0.66\ e^-$ was calculated for the OH groups (Table 2), which prefer to coordinate the protruding Fe_A ion at 1.92 and 1.95 Å for $HAsO_4^{2-}$ and HPO_4^{2-}, respectively (Figure. A.11).

Figure A.11 displays the radial distribution functions for $H_2PO_4^-$, HPO_4^{2-}, $H_2AsO_4^-$, and $HAsO_4^{2-}$, where the radii are measured from the central atom of the P or As solute

491 to the O of the water molecules. The main hydration shells for these oxyanions lie
492 between 3.5 and 6.0 Å, which is in excellent agreement with the molecular dynamics
493 (MD) simulations of Pathak and Bandyopadhyay (2016) for AsO_4^{3-} and supports the
494 suitability of the size of our water simulation box (Pathak and Bandyopadhyay, 2016).
495 Under acid conditions, the di-protonated arsenate ($H_2AsO_4^-$) and phosphate ($H_2PO_4^-$)
496 ions are the dominant species with C_{2v} symmetry and 15 fundamental vibrational
497 modes. Alkaline pH values lead to the deprotonation of the outer-sphere complexes,
498 thus increasing their symmetry to the C_{3v} molecular point group, with a reduction to 3
499 singly degenerate vibrations for the H atom. Generally, most of the fundamental
500 vibrational modes for As-containing anions are red-shifted with respect to their
501 phosphate counterparts, in excellent agreement with the ATR-FTIR experiments
502 (Table 3). The only exceptions are the stretching ν(PO−H) and bending δ(POH) mode
503 for HPO_4^{2-} and $H_2PO_4^-$, respectively, which appear at higher wavenumbers than for
504 the iso-structural As-based molecules. However, taking into account that the bending
505 δ(POH) is 1245 cm^{-1} for $H_2PO_4^-$ at acid pH (Table 3), which compares closely with
506 the experimental value of 1240 cm^{-1} (Figure. A.8), we are confident of the predictive
507 accuracy and consistency of our approximate vibrational modes. More details about
508 the DFT results of outer-sphere complexes are described in Text. A.4.
509
510 Arsenate adsorption on the Fe_3O_4(001) surface
511 The dissociative adsorption process of the $H_2AsO_4^-$ solute onto the Fe_3O_4 (001)
512 surface at acid pH can be represented as Eq. (5):

513 $$Fe_{24}O_{32}(001)(s) + H_2AsO_4(aq) = Fe_{24}O_{31}(001).OH.HAsO_4(s). \quad (5)$$

514 $HAsO_4^{2-}$ in the BB configuration is the most thermodynamically stable inner-sphere
515 complex calculated for arsenate (Figure. 5a), with the largest adsorption energy of
516 -2.19 eV per molecule (Table 2). The surface Fe_B ions coordinate the adsorbate O
517 atoms at 2.06 Å, which reduces their electronic density and induces an elongation of
518 the As=O bond distances by 0.03 Å with respect to the outer-sphere complexes. The
519 O−As=O and particularly the O=As=O bond angles become narrower after adsorption,
520 but the latter still remains wider than the former (Table 1). The dissociated proton
521 binds a neighboring surface O atom at 1.02 Å, which is a slightly larger bond distance
522 than in any of the other discussed solutes. The computed As-O bond length and As-Fe
523 distance of the BB arsenate complex are ca. 1.71 and 3.20 Å, respectively, which is
524 consistent with the values (1.69 and 3.42 Å) obtained from EXAFS analysis (Jonsson
525 and Sherman, 2008).
526 The acid proton has a typical charge of 0.67 e^-, while the inner-sphere complexes gain
527 0.60 e^- compared to the di-protonated molecule in solution. Consistent with the
528 presence of two types of H atoms, *i.e.,* in the inner-sphere complexes and directly
529 attached to the surface, six singly degenerate vibrational modes associated with these
530 atoms are found (Table 3). The stretching ν(AsO−H) and bending δ(AsOH) in the
531 adsorbed molecule are red-shifted with regard to the outer-sphere complexes, in line
532 with their different chemical environments. The stretching modes involving the
533 central As atom have the typical pattern of BB complexes. For instance, the largest
534 wavenumber of 816 cm^{-1} is assigned to the As=O bond, whereas the intermediate

vibrations between 751 and 786 cm^{-1} are calculated for the symmetric and asymmetric ν(As−OFe). In agreement with its largest distance, the softer mode is computed for the single bond between the central atom and the protonated oxygen.

Unlike the outer-sphere $H_2AsO_4^-$ complexes, which adsorb dissociatively in acid environment, the $HAsO_4^{2-}$ anion does not change its stoichiometry after binding to the Fe_3O_4(001) surface at alkaline pH (Eq. (6)):

$$Fe_{24}O_{32}(001).OH(s) + HAsO_4(aq) = Fe_{24}O_{32}(001).OH.HAsO_4(s). \quad (6)$$

The mono-protonated adsorbed As-containing molecule interacts with two Fe_B surface ions, forming a bidentate (BB) configuration that resembles the inner-sphere complexes of arsenate at acid pH (Figure. 5b).

However, the presence of an adsorbed OH^- group rather than H^+ causes noticeable energetic and structural changes in the adsorbate. The adsorption energy increases by 1.35 eV per $HAsO_4^{2-}$ molecule when the pH changes from acid to alkaline, becoming comparable to the experimental value reported by Sabur and coworkers for arsenate at neutral pH conditions (Sabur et al., 2015). The Fe_B−O bonds between the molecule and surface are 0.07 Å shorter at high than at low pH. The bond distance from the central As atom to the hydroxy group is stretched from 1.76 to 1.86 Å following the increase in pH. After adsorption, the adsorbed OH group moves 0.08 Å away from the surface and leans towards a nearby surface O atom to form a hydrogen bond. Table 1 shows that the relative order ∠(O−As=O) < ∠(O=As=O) is restored for the bond angles upon the formation of the inner-sphere complexes. Despite the same stoichiometry, the Bader charge analysis reveals that the adsorbate loses 0.14 e^- after

adsorption, but the charge of the OH^- remains almost unaffected at -0.68 e^-.

Owing to the similar adsorption configuration for $HAsO_4^{2-}$ at both acid and alkaline pH, the number and type of fundamental vibrational modes in these two conditions are the same. However, all vibrations shift for $HAsO_4^{2-}$ as a result of the change in pH (Table 3). For example, the wavenumber for ν(As−OH) increases greatly to 3007 cm^{-1}, whereas ω(AsOH) is red-shifted to 830 cm^{-1}. The increase in pH has a strong impact on the stretching mode of the elongated As−OH bond of the surface-immobilized $HAsO_4^{2-}$species. Moreover, the formation of the inner-sphere arsenate complexes and FeOH···H hydrogen bond have a major effect on the ν(FeO−H) and ω(FeOH) modes. Our DFT predicted vibrational frequencies for the hardest modes ν(As=O) and ν(As=OFe) of the inner-sphere $HAsO_4^{2-}$ complex under both acid and alkaline conditions are under-estimated by ~60 cm^{-1} with respect to the experimental values. However, the deviation between the ATR-FTIR spectra and the simulated frequency is 90 and 190 cm^{-1} under acid and alkaline conditions, respectively, for the softer mode ν(As−OH).

Phosphate adsorption on the Fe_3O_4(001) surface

Among the various possible binding geometries of phosphate onto magnetite, the mono-protonated monodentate mononuclear (MMM) mode is the most stable adsorption configuration at acid pH, wherein the HPO_4^{2-} anion binds the Fe_B surface cation and releases 1.89 eV per molecule (Table 2 and Figure. 6a). The dissociative adsorption of $H_2PO_4^-$ on the Fe_3O_4(001) surface at acid conditions can be represented

by Eq. (7):

$$Fe_{24}O_{32}(001)(s) + H_2PO_4(aq) = Fe_{24}O_{31}(001)OH.HPO_4(s) \quad (7)$$

As shown in Figure. 6a, the dissociated proton prefers to interact at 0.98 Å with a nearby surface oxygen atom to form acid $Fe_{24}O_{31}(001).OH$ groups rather than H_3O^+ cations in solution. The strong chemisorption is characterized by the adsorbate-surface PO−Fe_B interatomic bond distance of 2.08 Å, which is only 0.02 Å larger than the O−Fe_B distance in the bulk of Fe_3O_4 (Table 1). The average P=O distances for the outer- and inner-sphere P-containing complexes are very close at acid pH. Compared to $H_2PO_4^-$ in solution, the P−O bond stretches, whereas the PO−H bond distance decreases by approximately 0.05 Å for the adsorbed HPO_4^{2-}. The O−P=O bond angle experiences the largest change, from 109.06° to 105.01°, given that the adsorbate loses half of its single bonded O atoms during the dissociative adsorption of $H_2PO_4^-$. The charge of the dissociated H is 0.65 e^-, while the adsorbed anion becomes 0.66 e^- more negative than its parent ion in solution (Table 2).

Dissociative adsorption of $H_2PO_4^-$ in the MMM configuration causes its molecular point group to reduce to C_s and to 12 the total number of fundamental vibrational modes. After binding to the surface, the POH wagging is not detected above 600 cm^{-1}, while the PO−H stretching is shifted to 3625 cm^{-1} and the POH bending is red-shifted by approximately 200 cm^{-1} (Table 3). In line with the new symmetry, the two largest stretching modes are assigned to $P=O_2$, whereas 942 cm^{-1} corresponds to P−OFe and the lowest wavenumber is calculated for the protonated O atom. For the dissociated proton, the FeO−H stretching as well as the FeOH bending and wagging were

obtained at the usual position for OH groups. The calculated vibrational frequencies were also underestimated for the inner-sphere phosphate complexes in acid conditions, with the largest discrepancy observed for the modes with the smallest wavenumber. For example, the simulated values for the hardest ν(P=O) modes were just 5 and 20cm^{-1} below the experimental frequencies; while the difference for the softer (softest) ν(P=OFe) [ν(P−OH)] mode was 60 (104) cm^{-1}.

Under alkaline conditions, HPO_4^{2-} prefers to adsorb dissociatively onto the Fe_3O_4(001) surface, forming the non-protonated bidentate binuclear (NBB) inner-sphere complex and liquid water as follows:

$$Fe_{24}O_{32}(001).OH(s) + HPO_4(aq) = Fe_{24}O_{32}(001).PO_4(s) + H_2O(l). \quad (8)$$

This process releases 0.69 eV per molecule, which is the weakest adsorption energy reported in this study (Table 2). Two O atoms from the anion coordinate the surface Fe_A and Fe_B ions at 1.91 and 1.95 Å, respectively (Table 1 and Figure. 6b). A small stretch in the P=O bond from the average value of 1.56 Å is also observed in those atoms directly interacting with the surface, whereas the bond angles remain perfectly tetrahedral at 109.44°. The Bader charge for the inner-sphere PO_4^{3-} complex is −2.13 e^-, which is the largest reported in this paper. The charge of the fully deprotonated phosphate ion explains its small adsorption energy, caused by the strong Coulombic repulsion at the negatively charged Fe_3O_4(001) surface. The PZC of magnetite at 6.8 suggests that at alkaline pH, the Fe_3O_4 surfaces become negative due to adsorbed OH^- groups.

Despite its C_s point group, the adsorbed NBB PO_4^{3-} species has the simplest set of

623 vibrational frequencies with only 4 measurable fundamental modes (Table 3). The
624 largest frequencies are for the asymmetric and symmetric P=O modes, at 1111.64 and
625 948.85 cm^{-1}, respectively. The longest and weakest P−OFe bonds are characterized by
626 the smallest frequencies, which were calculated at 909 and 884 cm^{-1} for the
627 asymmetric and symmetric modes, respectively.
628 Although phosphate OS complexes are smaller than their arsenate counterparts (Table
629 1), the three solvation shells found are formed roughly at the same distance from the
630 central atom for the two different oxyanions, which essentially remain tetrahedral.
631 However, when the phosphate and arsenate molecules approach the Fe_3O_4(001)
632 surface, they form IS complexes of different geometries and number of interactions
633 with the exposed Fe ions. The adsorption energies show that under both acid and
634 alkaline conditions arsenate prefers to form MBB complexes with two neighboring
635 Fe_B ions from the Fe_3O_4(001) surface. However, phosphate forms an NBB complex
636 with the exposed Fe_A and Fe_B ions at alkaline pH, while HPO_3^{2-} coordinates a single
637 Fe_B ion as an MMM species under acid conditions (Figures. 6 and 7). On
638 thermodynamic grounds, arsenate species bind more strongly to the Fe_3O_4(001)
639 surface than the phosphate complexes under acid and alkaline conditions (Table 2),
640 which explains the stronger adsorption affinity of arsenate over phosphate. The
641 oxyanions release the largest adsorption energies under acid conditions and the
642 calculated Bader charges explain the trends found for the adsorption energies.
643 Adsorption reduces the molecular point group of the oxyanions, which impacts the
644 frequency of the four stretching modes involving the central atom and the oxygen

645 atoms (Table 3). The shift of the vibrational modes for the adsorbed oxyanions with
646 respect to the OS complexes offers an unambiguous route to characterize the
647 geometry and coordination number of the IS species.
648
649 Effect of pH on individual and comparative adsorption
650 During individual molecular adsorption of equal amounts of arsenate and phosphate,
651 their adsorption edges have very similar curve profiles, in agreement with previous
652 works (Arai and Sparks, 2001; Jia et al., 2007; Luengo et al., 2006). In this study, the
653 arsenate and phosphate adsorption increased gradually on magnetite as the pH
654 decreased (Figures. A.3 and A.6), ascribed to the positive charge of the mineral
655 surface. Such variations have also been observed in the individual adsorption of
656 arsenate and phosphate onto goethite, which is the most studied mineral adsorbent
657 (Hingston et al., 1971; Liu et al., 2001; Manning and Goldberg, 1996). As reported by
658 Liu et al., the surface coverage of phosphate and arsenate on goethite was 112 and 109
659 mol kg^{-1} at pH = 8, respectively, which values increased to 193 and 197 mol kg^{-1} at
660 pH = 3. Although the individual arsenate and phosphate adsorption showed similar
661 dependence on the pH, the binding efficiency was greatly affected by pH during
662 competitive adsorption. In this study, when pre-adsorbed on magnetite, 32% of
663 phosphate was desorbed in the presence of arsenate at pH = 4 (Figure. 5), while only
664 15% was desorbed at pH = 9 (Figure. 7). The phosphate adsorption strength increased
665 with pH, which was also observed during adsorption onto goethite and ferrihydrite.
666 Liu et al. found that, in the presence of arsenate, the efficiency of phosphate

adsorption on goethite increased from 50% (pH = 3) to 70% (pH = 8) and was not significantly influenced at alkaline pH, i.e., 69% (pH = 7), 70% (pH = 8) and 72% (pH = 9) (Liu et al., 2001). In order to evaluate the ability of phosphate (or arsenate) to depress the adsorption of arsenate (or phosphate) during competitive adsorption, the competition efficiency (%) of phosphate η_P was calculated as $\eta_P = 100 \times(1-N_{arsenate}/N^{o}_{arsenate})$, where $N_{arsenate}$ was the amount of arsenate adsorbed in the presence of phosphate and $N^{o}_{arsenate}$ was the amount of arsenate individually adsorbed (Liu et al., 2001). The obtained results show that, independently of pH, the competition efficiency of arsenate over phosphate ranged from 70 to 74%. In contrast, phosphate was more stable under alkaline than acid conditions.

The pH effect on the competitive adsorption efficiency between phosphate and arsenate has been observed in previous studies. For example, in soils, the inhibitory effect of phosphate toward arsenate adsorption is stronger than the other way round when the pH is higher than 6 (Melamed et al., 1995; Peryea, 1991). Gao and Mucci reported that the phosphate introduction obviously restrained the arsenate adsorption on goethite at alkaline pH. The arsenate addition, even in excess, led to only slight decrease in the amount of phosphate adsorbed (Gao and Mucci, 2001). These findings are different from ours, where the individual arsenate and phosphate adsorptions were found to be comparable at alkaline pH. However, the affinity towards goethite is stronger for arsenate than for phosphate at acid pH (Carabante et al., 2009; Violante and Pigna, 2002; Zhao and Stanforth, 2001), which becomes comparable under neutral conditions (Manning and Goldberg, 1996). Therefore, pH plays a vital role in

689 the competitive adsorption between arsenate and phosphate.

690

691 Effect of adsorption sequence on individual and comparative adsorption

692 The simultaneous or successive addition of oxyanions is important in the context of
693 competitive adsorption (Carabante et al., 2010; Liu et al., 2001). In nature,
694 environmental substances are more commonly adsorbed onto minerals sequentially
695 than simultaneously. When pre-adsorbed arsenate was replaced by phosphate on
696 goethite, the competition efficiency of arsenate and phosphate remained constant at
697 70–74% and 20%, respectively, independent of pH (Liu et al., 2001). However,
698 substitution of pre-adsorbed phosphate by arsenate led to an increase of the
699 competition efficiency of phosphate from 50% (acid pH) to 65% (alkaline pH), while
700 arsenate decreased from 30% (acid pH) to 10% (neutral pH). For the simultaneous
701 addition of the adsorbates, the efficiency of arsenate and phosphate was 50% and 40%,
702 respectively. Although the competitive adsorption experiment was carried out using
703 different adsorption sequences, arsenate was always adsorbed more strongly than
704 phosphate, indicating that arsenate has the highest affinity towards the goethite
705 surfaces. This was also found during the competitive arsenate and phosphate
706 adsorption onto magnetite and ferrihydrite (Carabante et al., 2010). For example, as
707 reported in this study, the amount of phosphate adsorbed decreased by 32% after the
708 introduction of arsenate at equal concentration under acid conditions. Conversely, the
709 subsequent addition of phosphate only resulted in about 10% arsenate desorption.
710 This is consistent with the results from the DFT calculations, where it was found that

711 arsenate has stronger adsorption affinity to magnetite than phosphate.

712

713 Effect of mineral species on individual and comparative adsorption

714 Diverse competitive adsorption trends appear for phosphate and arsenate during
715 interaction with different mineral phases in soils. In general, the competitive ability
716 towards iron (hydr)oxides is stronger for arsenate than for phosphate. As mentioned
717 above, during the adsorption on ferrihydrite and goethite, the restraining effect of
718 arsenate on phosphate is obviously the strongest. A similar phenomenon is also seen
719 in this study, where arsenate has higher affinity for and stability on magnetite than
720 phosphate. However, the opposite was found when aluminum (hydr)oxides were the
721 mineral phases. Manning et al. investigated competitive adsorption of arsenate and
722 phosphate on goethite and gibbsite (Manning and Goldberg, 1996). On both mineral
723 phases, phosphate induced the desorption of *ca.* 15mmol kg^{-1} of arsenate. However,
724 the arsenate addition only decreased the phosphate adsorption by 8mmol kg^{-1} on
725 gibbsite, which indicates a preference for phosphate rather than arsenate. ~~The~~
726 Arsenate and phosphate also display similar competitive adsorption on calcite ~~and~~
727 ~~aluminum (hydr)oxides~~. The arsenate adsorption is significantly inhibited by
728 phosphate, while the phosphate adsorption is barely affected by arsenate (So et al.,
729 2012).

730 In addition to the chemical formula of the mineral phases, the competitive adsorption
731 properties of arsenate and phosphate are also affected by the crystallinity of the
732 material. Xu et al. studied the effect of arsenate addition on the phosphate desorption

733 kinetics from crystalline and amorphous hydrargillite (Xu et al., 2008). Phosphate was
734 easily replaced by arsenate, which had the largest affinity for amorphous rather than
735 for crystalline hydrargillite, because of difference in the density of surface active sites.
736
737 Competitive adsorption mechanism
738 Despite the similar individual adsorption behavior, the mechanism for the competitive
739 adsorption between arsenate and phosphate onto the iron (hydr)oxide surfaces is still a
740 topic of debate. Phosphate with its smaller thermochemical radius is expected to have
741 the strongest affinity for these mineral phases, yet arsenate displays the strongest
742 preference, especially at acid pH.
743 During arsenate and phosphate adsorption onto iron (hydr)oxides, these oxyanions
744 adopt diverse geometries with different binding strengths. For example, phosphate
745 adsorbed on ferrihydrite displays two adsorption geometries, i.e., protonated BB and
746 non-protonated BB, as observed by *in situ* ATR-FTIR (Carabante et al., 2010).
747 Arsenate is mainly adsorbed in the BM and BB geometries, as determined by *in situ*
748 ATR-FTIR and XAFS (Carabante et al., 2010; Neupane et al., 2014). However, these
749 adsorption complexes display different affinities towards mineral surfaces. For
750 example, phosphate induces the desorption of the BM arsenate complexes, while the
751 BB arsenate complexes are less affected (Neupane et al., 2014), which indicates that
752 the stability is higher for the BB than for the BM arsenate species.
753 In this study, *in situ* ATR-FTIR and DFT calculations have revealed that phosphate
754 was individually adsorbed onto magnetite in the NBB and MMM geometries, while

arsenate mainly formed BB complexes with few OS species. However, under competitive adsorption conditions, the BB arsenate complexes obviously substituted both the MMM and to a lesser extent the NBB phosphate complexes. These findings illustrate that NBB phosphate complexes are more stable than MMM complexes, and also that their binding strength is weaker than for the BB arsenate complexes. The competitive adsorption of phosphate and arsenate can be explained by variations in adsorption geometries with pH. Under acid conditions, the dominant MMM phosphate species had the smallest adsorption energies (E_{ads} = -0.69 eV, Table 2) and were easily replaced by arsenate (E_{ads} = -0.84 eV). As pH increased, NBB became the main phosphate species, displaying enhanced stability (E_{ads} = -1.89 eV), which resulted in decreasing desorption by arsenate. Throughout the studied pH range, the adsorbed arsenate remained in the BB geometry with higher stability than phosphate. Thus, the competitive efficiency for phosphate increased with pH, while for arsenate it remained almost stable. These results for magnetite are in excellent agreement with the findings on goethite (Liu et al., 2001).

Besides the adsorption geometry, the Coulombic interaction between the positively charged magnetite surfaces and negatively charged adsorbates is another important factor controlling the competitive adsorption between arsenate and phosphate. Given the magnetite PZC at 6.8, the electrostatic attraction with phosphate and arsenate oxyanions increases as pH decreases. This improves the adsorption onto the magnetite surface and thus, decreases the proportion of hydroxyl groups covering adsorption sites. The adsorption geometry of phosphate species changes from NBB to MMM

777 complexes, which contain fewer protons. A similar variation in adsorption
778 complexation from binuclear to mononuclear is also observed during the adsorption
779 of arsenate onto ferrihydrite (Neupane et al., 2014). To form BB complexes with
780 higher stability than MM configurations, the oxyanions should be bound to two
781 adjacent protonated oxygen sites. However, only mononuclear complexes are formed
782 if the protonated oxygen site is far away from the adsorbate. Based on the shorter
783 intramolecular O···O distance in phosphate compared to arsenate (2.45 and 2.6–2.8 Å,
784 respectively), the latter is more likely to form BB complexes than the former (So et al.,
785 2012). Lumsdon et al. found that the interaction with hydroxyl sites was stronger for
786 arsenate than for phosphate, because of the different molecular sizes of the adsorbates
787 (Lumsdon et al., 1984). Thus, arsenate bidentate binuclear complexes dominate in
788 areas of high surface coverage, whereas monodentate species are only found in areas
789 of low surface coverage (Fendorf et al., 1997). In contrast, the large surface coverage
790 of phosphate species prefers the formation of monodentate complexes (Liu et al.,
791 2001), which was also found under the acidic condition in this study.
792 Compared to other iron oxides, the formation of abundant monodentate mononuclear
793 phosphate complexes on magnetite alongside a low proportion of arsenate OS species
794 is unique for this combination of substrate and adsorbates. The PZC value for
795 magnetite (~6.8) is lower than for goethite (~9.1), ferrihydrite (~7.6-8.1) or hematite
796 (~11), which leads to Fe_3O_4 displaying a lower degree of protonation than other iron
797 oxides at the same pH. Protonated surface sites facilitate IS surface complexation
798 because water is more easily displaced than hydroxyl groups (Johnston and

799 Chrysochoou, 2012). Thus, the decrease of protonation on the magnetite surface
800 results in the formation of more MM complexes of phosphate with fewer hydroxyl
801 groups, as well as OS species of arsenate. Similar variations have appeared in sulfate
802 adsorption, where IS complexes are exclusively found on hematite with the highest
803 PZC (Hug, 1997), and both OS and IS complexes are formed on ferrihydrite
804 (Johnston and Chrysochoou, 2014).
805
806 **IMPLICATIONS**
807 This study provides a molecular-level insight into the competitive adsorption between
808 arsenate and phosphate on magnetite surfaces. Magnetite has a widespread occurrence
809 in surface environment and is found coating the zero-valent iron nanoparticles
810 increasingly used for environmental engineering, especially for As removal. Thus, our
811 new results would be beneficial for assessing the environmental fate of arsenate and
812 phosphate, as well as for other ions that may compete for or otherwise react with the
813 magnetite surface sites.
814 Owing to the low surface site density of magnetite, its adsorption towards oxyanions
815 has seldom been surveyed by *in situ* techniques. In this study, with the aid of 2D-COS
816 analysis, we have resolved better the peaks of *in situ* ATR-FTIR spectra, which
817 greatly facilitates the identification of adsorption species and geometries of both
818 oxyanions. For phosphate, MMM complexes dominated at acid pH, while NBB
819 complexes were dominant at alkaline conditions. Arsenate mainly formed BB
820 complexes with some outer-sphere species, both of which were more prevalent at acid

than at alkaline pH. This is somewhat different from the cases on other iron oxides, e.g., ferrihydrite and goethite, ascribed to the lower surface site density of magnetite. The competitive adsorption of these adsorption species was further investigated by ATR-FTIR for different substitution sequences, providing spectroscopic evidence for their adsorption affinity towards magnetite surface. The adsorption strength was also thermodynamically confirmed for the first time through DFT calculations. Therefore, this study offers an important step forward in understanding the adsorption of oxyanions in complex systems, which is more environmentally realistic.

The adsorption affinity of the geometries as observed increased in the following order: MMM phosphate complex < NBB phosphate complex < BB arsenate complex. The high stability of adsorbed arsenate suggests the vital role of magnetite in the transfer and transformation of arsenic in surface environment. Meanwhile, magnetite could be used as an arsenic scavenger for *in situ* remediation of phosphate-rich groundwater and soil.

ACKNOWLEDGEMENTS

This work was financially supported by the National Key Research and Development Program of China (Grant No. 2017YFC0602306), the National Natural Science Foundation of China (Grant Nos. 41773113 and 41825003), Natural Science Foundation for Distinguished Young Scientists of Guangdong Province (Grant No. 2020B1515020015), Science and Technology Program of Guangzhou, China (Grant No. 201804020037), and the Youth Innovation Promotion Association CAS (Grant No. Y201863). D.S.-C. and N.H.d.L. acknowledge the Engineering and Physical Sciences Research Council (EPSRC, Grant No. EP/K009567) for funding. *Via* our membership of the UK's HEC Materials Chemistry Consortium, which is funded by EPSRC (Grant No. EP/L000202 and EP/R029431), this work used the ARCHER UK National Supercomputing Service (http://www.archer.ac.uk). This work also used the computational facilities of the Advanced Research Computing @ Cardiff (ARCCA) Division, Cardiff University. This research was undertaken using the Supercomputing Facilities at Cardiff University operated by ARCCA on behalf of the Cardiff Supercomputing Facility, HPC Wales and Supercomputing Wales (SCW) projects. We acknowledge the support of the latter, which is part-funded by the European Regional Development Fund (ERDF) *via* Welsh Government. All data created during this research is openly available from the Cardiff University's Research Portal at http://doi.org/10.17035/d. 2019.0081529534.

Appendix A. Supplementary material

Supplementary data associated with this article can be found in the online version, at XXX.

858 **REFERENCES CITED**

859 Anisimov, V.I., Korotin, M.A., Zaanen, J., and Andersen, O.K. (1992) Spin Bags,
860 Polarons, and Impurity Potentials in $La_{2-x}Sr_xCuO_4$ from 1st Principles.
861 Physical Review Letters, 68(3), 345-348.

862 Antelo, J., Arce, F., and Fiol, S. (2015) Arsenate and phosphate adsorption on
863 ferrihydrite nanoparticles. Synergetic interaction with calcium ions. Chemical
864 Geology, 410, 53-62.

865 Arai, Y., and Sparks, D.L. (2001) ATR-FTIR spectroscopic investigation on
866 phosphate adsorption mechanisms at the ferrihydrite-water interface. Journal
867 of Colloid and Interface Science, 241(2), 317-326.

868 Blochl, P.E. (1994) Projector Augmented-Wave Method. Physical Review B, 50(24),
869 17953-17979.

870 Brechbuhl, Y., Christl, I., Elzinga, E.J., and Kretzschmar, R. (2012) Competitive
871 sorption of carbonate and arsenic to hematite: Combined ATR-FTIR and batch
872 experiments. Journal of Colloid and Interface Science, 377, 313-321.

873 Carabante, I., Grahn, M., Holmgren, A., and Hedlund, J. (2010) In situ ATR-FTIR
874 studies on the competitive adsorption of arsenate and phosphate on ferrihydrite.
875 Journal of Colloid and Interface Science, 351(2), 523-531.

876 Carabante, I., Grahn, M., Holmgren, A., Kumpiene, J., and Hedlund, J. (2009)
877 Adsorption of As (V) on iron oxide nanoparticle films studied by in situ
878 ATR-FTIR spectroscopy. Colloids and Surfaces a-Physicochemical and
879 Engineering Aspects, 346(1-3), 106-113.

880 Catalano, J.G., Park, C., Fenter, P., and Zhang, Z. (2008) Simultaneous inner- and
881 outer-sphere arsenate adsorption on corundum and hematite. Geochimica Et
882 Cosmochimica Acta, 72(8), 1986-2004.
883 Chakraborti, D., Rahman, M.M., Paul, K., Chowdhury, U.K., Sengupta, M.K., Lodh,
884 D., Chanda, C.R., Saha, K.C., and Mukherjee, S.C. (2002) Arsenic calamity in
885 the Indian subcontinent - What lessons have been learned? Talanta, 58(1),
886 3-22.
887 Choppala, G., Bolan, N., Kunhikrishnan, A., and Bush, R. (2016) Differential effect
888 of biochar upon reduction-induced mobility and bioavailability of arsenate and
889 chromate. Chemosphere, 144, 374-381.
890 Correll, D.L. (1998) The role of phosphorus in the eutrophication of receiving waters:
891 A review. Journal of Environmental Quality, 27(2), 261-266.
892 Dudarev, S.L., Botton, G.A., Savrasov, S.Y., Humphreys, C.J., and Sutton, A.P.
893 (1998) Electron-energy-loss spectra and the structural stability of nickel oxide:
894 An LSDA+U study. Physical Review B, 57(3), 1505-1509.
895 Dupuis, C., and Beaudoin, G. (2011) Discriminant diagrams for iron oxide trace
896 element fingerprinting of mineral deposit types. Mineralium Deposita, 46(4),
897 319-335.
898 Elzinga, E.J., and Sparks, D.L. (2007) Phosphate adsorption onto hematite: An in situ
899 ATR-FTIR investigation of the effects of pH and loading level on the mode of
900 phosphate surface complexation. Journal of Colloid and Interface Science,
901 308(1), 53-70.

902 Fendorf, S., Eick, M.J., Grossl, P., and Sparks, D.L. (1997) Arsenate and chromate
903 retention mechanisms on goethite .1. Surface structure. Environmental Science
904 & Technology, 31(2), 315-320.
905 Filip, J., Karlicky, F., Marusak, Z., Lazar, P., Cernik, M., Otyepka, M., and Zboril, R.
906 (2014) Anaerobic reaction of nanoscale zerovalent iron with water:
907 Mechanism and kinetics. Journal of Physical Chemistry C, 118(25),
908 13817-13825.
909 Gao, X.D., Root, R.A., Farrell, J., Ela, W., and Chorover, J. (2013) Effect of silicic
910 acid on arsenate and arsenite retention mechanisms on 6-L ferrihydrite: A
911 spectroscopic and batch adsorption approach. Applied Geochemistry, 38,
912 110-120.
913 Gao, Y., and Mucci, A. (2001) Acid base reactions, phosphate and arsenate
914 complexation, and their competitive adsorption at the surface of goethite in 0.7
915 M NaCl solution. Geochimica Et Cosmochimica Acta, 65(14), 2361-2378.
916 Gorski, C.A., Nurmi, J.T., Tratnyek, P.G., Hofstetter, T.B., and Scherer, M.M. (2010)
917 Redox behavior of magnetite: Implications for contaminant reduction.
918 Environmental Science & Technology, 44(1), 55-60.
919 Grimme, S. (2006) Semiempirical GGA-type density functional constructed with a
920 long-range dispersion correction. Journal of Computational Chemistry, 27(15),
921 1787-1799.
922 Grossl, P.R., Eick, M., Sparks, D.L., Goldberg, S., and Ainsworth, C.C. (1997)
923 Arsenate and chromate retention mechanisms on goethite .2. Kinetic

924 evaluation using a pressure-jump relaxation technique. Environmental Science
925 & Technology, 31(2), 321-326.
926 Guo, H.B., and Barnard, A.S. (2013) Naturally occurring iron oxide nanoparticles:
927 morphology, surface chemistry and environmental stability. Journal of
928 Materials Chemistry A, 1(1), 27-42.
929 Han, J., and Ro, H.M. (2018) Interpreting competitive adsorption of arsenate and
930 phosphate on nanosized iron (hydr)oxides: effects of pH and surface loading.
931 Environmental Science and Pollution Research, 25(28), 28572-28582.
932 Hashem, M.A., Toda, K., and Ohira, S.I. (2015) Leaching behavior of arsenite and
933 arsenate from the contaminated sediment by the effect of phosphate ion under
934 anaerobic conditions. Environmental Earth Sciences, 74(1), 745-745.
935 He, G.Z., Zhang, M.Y., and Pan, G. (2009) Influence of pH on initial concentration
936 effect of arsenate adsorption on TiO_2 surfaces: Thermodynamic, DFT, and
937 EXAFS interpretations. Journal of Physical Chemistry C, 113(52),
938 21679-21686.
939 Hiemstra, T. (2013) Surface and mineral structure of ferrihydrite. Geochimica Et
940 Cosmochimica Acta, 105, 316-325.
941 Hingston, F.J., Posner, A.M., and Quirk, J.P. (1971) Competitive adsorption of
942 negatively charged ligands on oxide surfaces. Discussions of the Faraday
943 Society, 52(0), 334-342.
944 Hu, S., Yan, W., and Duan, J.M. (2015) Polymerization of silicate on TiO_2 and its
945 influence on arsenate adsorption: An ATR-FTIR study. Colloids and Surfaces

946 a-Physicochemical and Engineering Aspects, 469, 180-186.
947 Hug, S.J. (1997) In situ Fourier transform infrared measurements of sulfate adsorption
948 on hematite in aqueous solutions. Journal of Colloid and Interface Science,
949 188(2), 415-422.
950 Jia, Y.F., Xu, L.Y., Wang, X., and Demopoulos, G.P. (2007) Infrared spectroscopic
951 and X-ray diffraction characterization of the nature of adsorbed arsenate on
952 ferrihydrite. Geochimica Et Cosmochimica Acta, 71(7), 1643-1654.
953 Johnston, C.P., and Chrysochoou, M. (2012) Investigation of chromate coordination
954 on ferrihydrite by in situ ATR-FTIR spectroscopy and theoretical frequency
955 calculations. Environmental Science & Technology, 46(11), 5851-5858.
956 -. (2014) Mechanisms of chromate adsorption on hematite. Geochimica Et
957 Cosmochimica Acta, 138, 146-157.
958 Jonsson, J., and Sherman, D.M. (2008) Sorption of As(III) and As(V) to siderite,
959 green rust (fougerite) and magnetite: Implications for arsenic release in anoxic
960 groundwaters. Chemical Geology, 255(1-2), 173-181.
961 Kanematsu, M., Young, T.M., Fukushi, K., Green, P.G., and Darby, J.L. (2010)
962 Extended Triple Layer Modeling of Arsenate and Phosphate Adsorption on a
963 Goethite-based Granular Porous Adsorbent. Environmental Science &
964 Technology, 44(9), 3388-3394.
965 Kocourkova-Vikova, E., Loun, J., Sracek, O., Houzar, S., and Filip, J. (2015)
966 Secondary arsenic minerals and arsenic mobility in a historical waste rock pile
967 at Kank near Kutna Hora, Czech Republic. Mineralogy and Petrology, 109(1),

968 17-33.
969 Kresse, G., and Furthmuller, J. (1996a) Efficiency of ab-initio total energy
970 calculations for metals and semiconductors using a plane-wave basis set.
971 Computational Materials Science, 6(1), 15-50.
972 -. (1996b) Efficient iterative schemes for ab initio total-energy calculations using a
973 plane-wave basis set. Physical Review B, 54(16), 11169-11186.
974 Kresse, G., and Hafner, J. (1993) Abinitio Molecular-Dynamics for Liquid-Metals.
975 Physical Review B, 47(1), 558-561.
976 -. (1994) Ab-Initio Molecular-Dynamics Simulation of the Liquid-Metal
977 Amorphous-Semiconductor Transition in Germanium. Physical Review B,
978 49(20), 14251-14269.
979 Kresse, G., and Joubert, D. (1999) From ultrasoft pseudopotentials to the projector
980 augmented-wave method. Physical Review B, 59(3), 1758-1775.
981 Krumina, L., Kenney, J.P.L., Loring, J.S., and Persson, P. (2016) Desorption
982 mechanisms of phosphate from ferrihydrite and goethite surfaces. Chemical
983 Geology, 427, 54-64.
984 Kubicki, J.D., Paul, K.W., Kabalan, L., Zhu, Q., Mrozik, M.K., Aryanpour, M.,
985 Pierre-Louis, A.M., and Strongin, D.R. (2012) ATR-FTIR and density
986 functional theory study of the structures, energetics, and vibrational spectra of
987 phosphate adsorbed onto goethite. Langmuir, 28(41), 14573-14587.
988 Kunhikrishnan, A., Choppala, G., Seshadri, B., Wijesekara, H., Bolan, N.S., Mbene,
989 K., and Kim, W.-I. (2017) Impact of wastewater derived dissolved organic

carbon on reduction, mobility, and bioavailability of As (V) and Cr (VI) in contaminated soils. Journal of Environmental Management, 186(2), 183-191.

Liang, X.L., Wei, G.L., Xiong, J., Tan, F.D., He, H.P., Qu, C.C., Yin, H., Zhu, J.X., Zhu, R.L., Qin, Z.H., and Zhang, J. (2017) Adsorption isotherm, mechanism, and geometry of Pb(II) on magnetites substituted with transition metals. Chemical Geology, 470, 132-140.

Liang, X.L., Zhong, Y.H., He, H.P., Yuan, P., Zhu, J.X., Zhu, S.Y., and Jiang, Z. (2012) The application of chromium substituted magnetite as heterogeneous Fenton catalyst for the degradation of aqueous cationic and anionic dyes. Chemical Engineering Journal, 191, 177-184.

Liang, X.L., Zhong, Y.H., Zhu, S.Y., He, H.P., Yuan, P., Zhu, J.X., and Jiang, Z. (2013) The valence and site occupancy of substituting metals in magnetite spinel structure $Fe_{3-x}M_xO_4$ (M = Cr, Mn, Co and Ni) and their influence on thermal stability: An XANES and TG-DSC investigation. Solid State Sciences, 15, 115-122.

Liu, C.H., Chuang, Y.H., Chen, T.Y., Tian, Y., Li, H., Wang, M.K., and Zhang, W. (2015) Mechanism of arsenic adsorption on magnetite nanoparticles from water: Thermodynamic and spectroscopic Studies. Environmental Science & Technology, 49(m13), 7726-7734.

Liu, F., De Cristofaro, A., and Violante, A. (2001) Effect of pH, phosphate and oxalate on the adsorption/desorption of arsenate on/from goethite. Soil Science, 166(3), 197-208.

1012 Livi, K.J.T., Villalobos, M., Leary, R., Varela, M., Barnard, J., Villacis-Garcia, M.,
1013 Zanella, R., Goodridge, A., and Midgley, P. (2017) Crystal Face Distributions
1014 and Surface Site Densities of Two Synthetic Goethites: Implications for
1015 Adsorption Capacities as a Function of Particle Size. Langmuir, 33(36),
1016 8924-8932.
1017 Loring, J.S., Sandstrom, M.H., Noren, K., and Persson, P. (2009) Rethinking arsenate
1018 coordination at the surface of goethite. Chemistry-a European Journal, 15(20),
1019 5063-5072.
1020 Luengo, C., Brigante, M., Antelo, J., and Avena, M. (2006) Kinetics of phosphate
1021 adsorption on goethite: Comparing batch adsorption and ATR-IR
1022 measurements. Journal of Colloid and Interface Science, 300(2), 511-518.
1023 Lumsdon, D.G., Fraser, A.R., Russell, J.D., and Livesey, N.T. (1984) New infrared
1024 band assignments for the arsenate ion adsorbed on synthetic goethite
1025 (α-FeOOH). Journal of Soil Science, 35(3), 381-386.
1026 Manning, B.A., and Goldberg, S. (1996) Modeling competitive adsorption of arsenate
1027 with phosphate and molybdate on oxide minerals. Soil Science Society of
1028 America Journal, 60, 121-131.
1029 Melamed, R., Jurinak, J.J., and Dudley, L.M. (1995) Effect of adsorbed phosphate on
1030 transport of arsenate through an oxisol. Soil Science Society of America
1031 Journal, 59(5), 1289-1294.
1032 Mermin, D.N. (1965) Thermal properties of the inhomogeneous electron gas. Physical
1033 Review, 137(5A), A1441-A1443.

1034 Mohan, D., and Pittman, C.U. (2007) Arsenic removal from water/wastewater using
1035 adsorbents - A critical review. Journal of Hazardous Materials, 142(1-2), 1-53.
1036 Neel, L. (1948) Proprietes Magnetiques Des Ferrites - Ferrimagnetisme Et
1037 Antiferromagnetisme. Annales De Physique, 3(2), 137-198.
1038 Neupane, G., Donahoe, R.J., and Arai, Y. (2014) Kinetics of competitive
1039 adsorption/desorption of arsenate and phosphate at the ferrihydrite-water
1040 interface. Chemical Geology, 368, 31-38.
1041 O'Reilly, S.E., Strawn, D.G., and Sparks, D.L. (2001) Residence time effects on
1042 arsenate adsorption/desorption mechanisms on goethite. Soil Science Society
1043 of America Journal, 65(1), 67-77.
1044 Ona-Nguema, G., Morin, G., Juillot, F., Calas, G., and Brown, G.E. (2005) EXAFS
1045 analysis of arsenite adsorption onto two-line ferrihydrite, hematite, goethite,
1046 and lepidocrocite. Environmental Science & Technology, 39(23), 9147-9155.
1047 Pathak, A.K., and Bandyopadhyay, T. (2016) Solvation of arsenate anion: combined
1048 quantum mechanics and molecular dynamics based investigation. Molecular
1049 Physics, 114(13), 2029-2036.
1050 Pedersen, H.D., Postma, D., Jakobsen, R., and Larsen, O. (2005) Fast transformation
1051 of iron oxyhydroxides by the catalytic action of aqueous Fe(II). Geochimica Et
1052 Cosmochimica Acta, 69(16), 3967-3977.
1053 Perdew, J.P., Burke, K., and Ernzerhof, M. (1996) Generalized gradient
1054 approximation made simple. Physical Review Letters, 77(18), 3865-3868.
1055 -. (1997) Generalized gradient approximation made simple (vol 77, pg 3865, 1996).

1056 Physical Review Letters, 78(7), 1396-1396.
1057 Peryea, F.J. (1991) Phosphate-induced release of arsenic from soils contaminated with
1058 lead arsenate. Soil Science Society of America Journal, 55(5), 1301-1306.
1059 Sabur, M.A., Goldberg, S., Gale, A., Kabengi, N., and Al-Abadleh, H.A. (2015)
1060 Temperature-Dependent Infrared and Calorimetric Studies on Arsenicals
1061 Adsorption from Solution to Hematite Nanoparticles. Langmuir, 31(9),
1062 2749-2760.
1063 Santos-Carballal, D., Roldan, A., Dzade, N.Y., and de Leeuw, N.H. (2018) Reactivity
1064 of CO_2 on the surfaces of magnetite (Fe_3O_4), greigite (Fe_3S_4) and mackinawite
1065 (FeS). Philosophical Transactions of the Royal Society a-Mathematical
1066 Physical and Engineering Sciences, 376(2110).
1067 Santos-Carballal, D., Roldan, A., Grau-Crespo, R., and de Leeuw, N.H. (2014) A
1068 DFT study of the structures, stabilities and redox behaviour of the major
1069 surfaces of magnetite Fe_3O_4. Physical Chemistry Chemical Physics, 16(39),
1070 21082-21097.
1071 Scott, T.B., Allen, G.C., Heard, P.J., and Randell, M.G. (2005) Reduction of U(VI) to
1072 U(IV) on the surface of magnetite. Geochimica Et Cosmochimica Acta, 69(24),
1073 5639-5646.
1074 Sherman, D.M., and Randall, S.R. (2003) Surface complexation of arsenie(V) to
1075 iron(III) (hydr)oxides: Structural mechanism from ab initio molecular
1076 geometries and EXAFS spectroscopy. Geochimica Et Cosmochimica Acta,
1077 67(22), 4223-4230.

1078 Shull, C.G., Wollan, E.O., and Koehler, W.C. (1951) Neutron Scattering and
1079 Polarization by Ferromagnetic Materials. Physical Review, 84(5), 912-921.
1080 Silva, and Fraustoda, J.R.R. (2001) The biological chemistry of the elements : the
1081 inorganic chemistry of life. 62-63 p. Clarendon Press.
1082 So, H.U., Postma, D., Jakobsen, R., and Larsen, F. (2012) Competitive adsorption of
1083 arsenate and phosphate onto calcite; experimental results and modeling with
1084 CCM and CD-MUSIC. Geochimica Et Cosmochimica Acta, 93, 1-13.
1085 Sprague, D.D., and Vermaire, J.C. (2018) Legacy Arsenic Pollution of Lakes Near
1086 Cobalt, Ontario, Canada: Arsenic in Lake Water and Sediment Remains
1087 Elevated Nearly a Century After Mining Activity Has Ceased. Water Air and
1088 Soil Pollution, 229(3).
1089 Sun, Z.X., Su, F.W., Forsling, W., and Samskog, P.O. (1998) Surface characteristics
1090 of magnetite in aqueous suspension. Journal of Colloid and Interface Science,
1091 197(1), 151-159.
1092 Swedlund, P.J., Holtkamp, H., Song, Y.T., and Daughney, C.J. (2014)
1093 Arsenate-ferrihydrite systems from minutes to months: A macroscopic and IR
1094 spectroscopic study of an elusive equilibrium. Environmental Science &
1095 Technology, 48(5), 2759-2765.
1096 Tamura, H., Katayama, N., and Furuichi, R. (1993) Modeling the ion-exchange
1097 adsorption of heavy-metal ions on the surface of metal-oxides. Bunseki
1098 Kagaku, 42(11), 719-724.
1099 Tejedortejedor, M.I., and Anderson, M.A. (1990) Protonation of phosphate on the

surface of goethite as studied by cir-FTIR and electrophoretic mobility. Langmuir, 6(3), 602-611.

Tiberg, C., Sjostedt, C., Persson, I., and Gustafsson, J.P. (2013) Phosphate effects on copper(II) and lead(II) sorption to ferrihydrite. Geochimica Et Cosmochimica Acta, 120, 140-157.

Villalobos, M., Cheney, M.A., and Alcaraz-Cienfuegos, J. (2009) Goethite surface reactivity: II. A microscopic site-density model that describes its surface area-normalized variability. Journal of Colloid and Interface Science, 336(2), 412-422.

Violante, A., and Pigna, M. (2002) Competitive sorption of arsenate and phosphate on different clay minerals and soils. Soil Science Society of America Journal, 66(6), 1788-1796.

WHO. (2011) Guidelines for Drinking-water Quality 4th Ed.

Winkel, L.H.E., Pham, T.K.T., Vi, M.L., Stengel, C., Amini, M., Nguyen, T.H., Pham, H.V., and Berg, M. (2011) Arsenic pollution of groundwater in Vietnam exacerbated by deep aquifer exploitation for more than a century. Proceedings of the National Academy of Sciences of the United States of America, 108(4), 1246-1251.

Xu, R.K., Kozak, L.M., and Huang, P.M. (2008) Kinetics of phosphate-induced desorption of arsenate adsorbed on crystalline and amorphous aluminum hydroxides. Soil Science, 173(10), 683-693.

Yan, W., Wang, H.B., and Jing, C.Y. (2016) Adhesion of Shewanella oneidensis

MR-1 to Goethite: A Two-Dimensional Correlation Spectroscopic Study. Environmental Science & Technology, 50(8), 4343-4349.

Zhang, J.H., Zhang, C.H., Wei, G.L., Li, Y., Liang, X.L., Chu, W., He, H.P., Huang, D.Y., Zhu, J.X., and Zhu, R.L. (2017a) Reduction removal of hexavalent chromium by zinc-substituted magnetite coupled with aqueous Fe(II) at neutral pH value. Journal of Colloid and Interface Science, 500, 20-29.

Zhang, L., Qin, X., Tang, J., Liu, W., and Yang, H. (2017b) Review of arsenic geochemical characteristics and its significance on arsenic pollution studies in karst groundwater, Southwest China. Applied Geochemistry, 77, 80-88.

Zhang, M.Y., Pan, G., Zhao, D.Y., and He, G.Z. (2011) XAFS study of starch-stabilized magnetite nanoparticles and surface speciation of arsenate. Environmental Pollution, 159(12), 3509-3514.

Zhao, H.S., and Stanforth, R. (2001) Competitive adsorption of phosphate and arsenate on goethite. Environmental Science & Technology, 35(24), 4753-4757.

Zhao, L.J., Zhang, H.J., Xing, Y., Song, S.Y., Yu, S.Y., Shi, W.D., Guo, X.M., Yang, H.H., Le, Y.Q., and Cao, F. (2008) Morphology-controlled synthesis of magnetites with nanoporous structures and excellent magnetic properties. Chemistry of Materials, 20(1), 198-204.

TABLES

TABLE 1. Adsorption sites, mean interatomic distances (*d*) and bond angles (∠) for the energetically preferred outer- (OS) and inner-sphere (IS) complexes of arsenate and phosphate at the Fe_3O_4 (001) surface in both acid and alkaline conditions.

Solute	pH	Adsorption site	[a]*d*(*X*−O)	*d*(*X*=O)	*d*(*X*O−H)	*d*(*X*O−Fe)	*d*(Fe−OH)	*d*(FeO−H)	∠(O−*X*−O)	∠(O−*X*=O)	∠(O=*X*=O)	∠(*X*OH)
			(Å)						(°)			
$H_2AsO_4^-$	acid	−	1.77	1.69	1.04	−	−	−	104.72	108.90	116.03	108.08
$HAsO_4$		Fe_B, Fe_B	1.76	1.72	1.05	2.06		1.02	−	107.31	111.54	112.97
$HAsO_4^{2-}$	alkaline	−	1.76	1.72	1.01	−	1.92	0.99	−	109.81	109.06	109.42
$HAsO_4$		Fe_B, Fe_B	1.82	1.71	1.01	2.00	2.00	0.99	−	104.45	114.00	106.64
$H_2PO_4^-$	acid	−	1.60	1.53	1.02	−	−	−	105.88	109.06	114.38	114.21
HPO_4		Fe_B	1.65	1.54	0.98	2.08	−	0.98	−	105.01	113.55	114.25
HPO_4^{2-}	alkaline	−	1.60	1.54	1.03	−	1.95	0.97	−	106.99	111.87	120.38
PO_4		Fe_A, Fe_B	−	1.56	−	1.93	−	−	−	−	109.44	−

[a]: *X* represents the central atom (P or As) of adsorbate.

TABLE 2. Adsorption sites, adsorption energies (E_{ads}) and charges (q) for the energetically preferred outer- (OS) and inner-sphere (IS) complexes of arsenate and phosphate at the Fe_3O_4 (001) surface in both acid and alkaline conditions.

Solute	pH	Adsorption site	E_{ads} (eV per molecule)	[a]$q(H_mXO_4)$ (e^-)	q(OH)	q(H)
$H_2AsO_4^-$	acid	–	–	−0.82	–	–
$HAsO_4$		Fe_B, Fe_B	−2.19	−1.42	–	0.67
$HAsO_4^{2-}$	alkaline	–	–	−1.52	−0.66	–
$HAsO_4$		Fe_B, Fe_B	−0.84	−1.38	−0.68	–
$H_2PO_4^-$	acid	–	–	−0.84	–	–
HPO_4		Fe_B	−1.89	−1.50	–	0.65
HPO_4^{2-}	alkaline	–	–	−1.54	−0.65	–
PO_4		Fe_A, Fe_B	−0.69	−2.13	–	–

[a]: *X* represents the central atom (P or As) of adsorbate. *m* indicates the degree of protonation of the solute, which can take integer values from 0 to 3.

TABLE 3. Molecular point groups, adsorption sites and wavenumbers of the fundamental vibrational modes for the energetically preferred outer- (OS) and inner-sphere (IS) complexes of arsenate and phosphate at the Fe_3O_4 (001) surface in both acid and alkaline conditions. The presented vibrational frequencies are stretching (ν), bending (δ) and wagging (ω).

Solute	pH	Sym	Adsorption site	ν(FeO−H)	[a]ν(*X*O−H)	δ(*X*OH)	ω(*X*OH)	ν(*X*=O)	ν(*X*−OH)	ν(*X*=OFe)	δ(FeOH)	ω(FeOH)
				(cm^{-1})								
$H_2AsO_4^-$	acid	C_{2v}	OS	−	3066	1372	1028	870	735	−	−	−
					2266	1268	756	817	666			
$HAsO_4^{2-}$		C_s	Fe_B, Fe_B	2875	2429	1291	1037	816	721	786	1042	1035
										751		
$HAsO_4^{2-}$	alkaline	C_{3v}	OS	3365	3120	1190	776	830	728	−	1060	721
								790				
								756				
$HAsO_4^{2-}$		C_s	Fe_B, Fe_B	3458	3007	1278	830	792	624	810	928	797
										782		
$H_2PO_4^-$	acid	C_{2v}	OS	−	2826	1269	938	1096	904	−	−	−
					2742	1221	920	1012	839			
HPO_4^{2-}		C_s	Fe_B	3350	3625	1018	−	1088	766	942	1170	706
								1045				
HPO_4^{2-}	alkaline	C_{3v}	OS	3739	2626	1271	947	1045	867	−	718	616
								1003				
								926				
PO_4^{3-}		C_s	Fe_A, Fe_B	−	−	−	−	1112	−	909	−	−
								949		884		

[a]: *X* represents the central atom (P or As) of adsorbate.

FIGURES

Figure.1

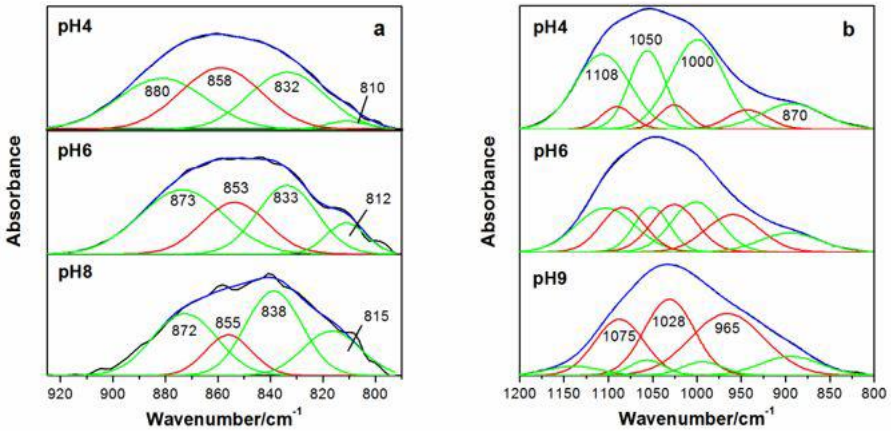

FIGURE 1. Infrared spectra for the individual adsorption of arsenate (a) and phosphate (b) on magnetite surface at acid, neutral and alkaline conditions, as well as the spectral fitting with different adsorption species (arsenate: inner-sphere (green line) and outer-sphere (red line) species; phosphate: monoprotonated monodentate-mononuclear (green line) and non-protonated bidentate-binuclear complexes (red line)). The total fit is represented by the blue line.

Figure.2

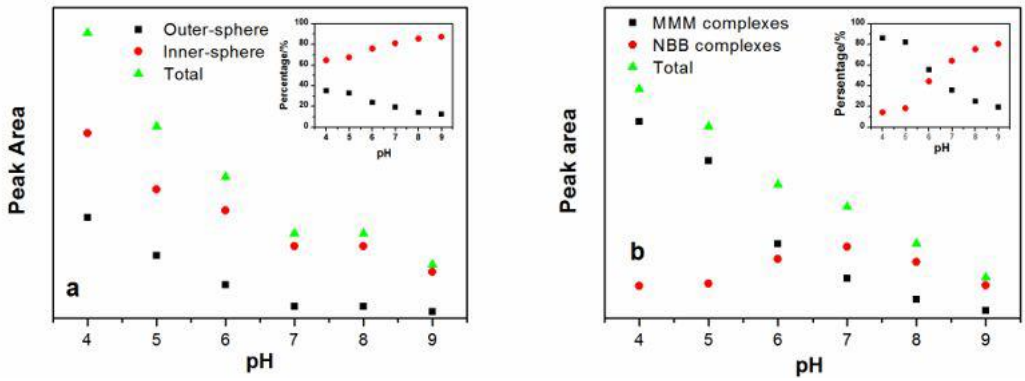

FIGURE 2. Integrated absorbance (IA) of the bands assigned to the adsorbed arsenate (a) and phosphate (b) plotted vs. pH, and the relative percentage of different adsorption species (arsenate: inner-sphere and outer-sphere species; phosphate:

monoprotonated monodentate-mononuclear (MMM) and non-protonated bidentate-binuclear (NBB) complexes).

Figure.3

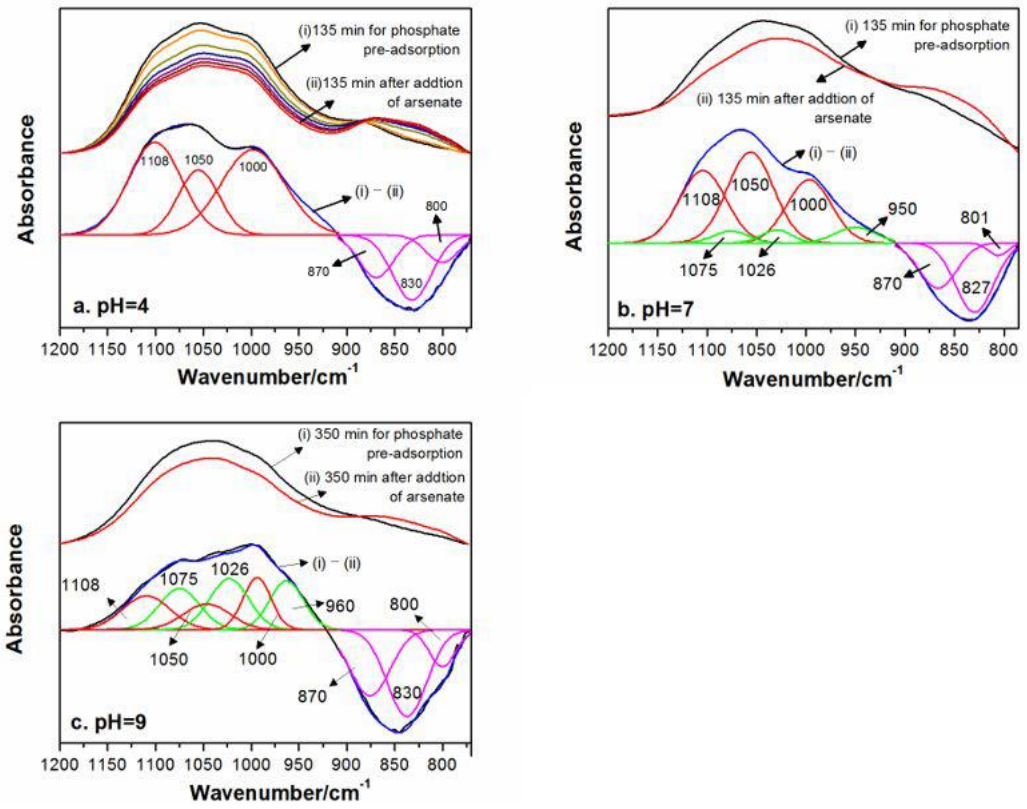

FIGURE 3. Infrared spectra of phosphate adsorbed onto magnetite at pH = 4 (a), pH = 7 (b) and pH = 9 (c). After 135 (a and b) or 350 (c) min, arsenate was added at an equal (molar) concentration and the spectral change was monitored for another 135 (a and b) or 350 (c) min.

Figure.4

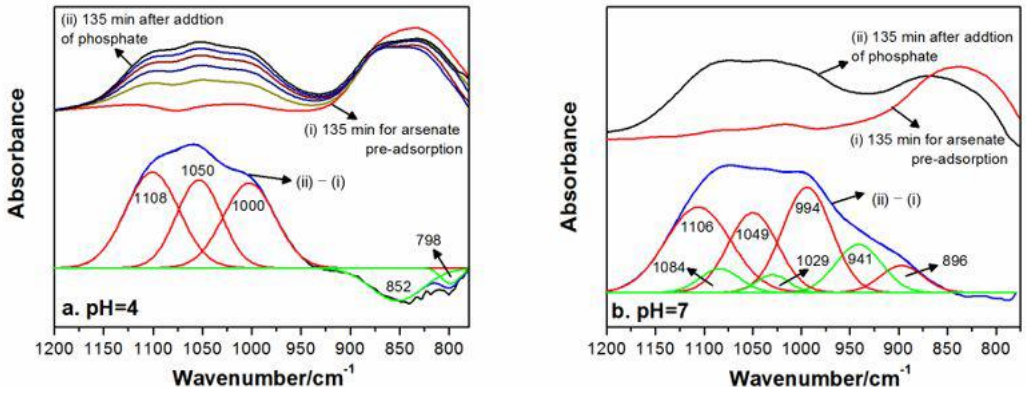

FIGURE 4. Infrared spectra of arsenate adsorbed onto magnetite at pH = 4 (a) and pH = 7 (b). After 135 min, a phosphate solution at an equal (molar) concentration was added and the spectral change was monitored for another 135 (a and b) min.

Figure.5.

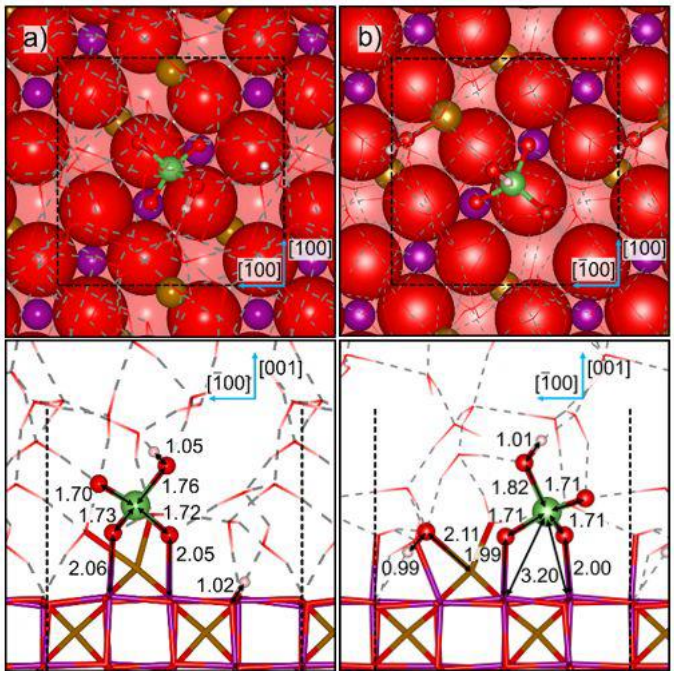

FIGURE 5. Top and side view of the aqueous inner-sphere species $HAsO_4^{2-}$ in (a) acid and (b) alkaline conditions. Tetrahedral Fe_A atoms are in orange, octahedral Fe_B atoms are in violet, O atoms are in red, As atoms are in green and H atoms are in pink. Surface atoms are represented as (top panels) balls and (bottom panels) sticks,

1187 water solvent molecules are represented as wireframe and the solute molecules are
1188 represented as balls-and-sticks. Light and dark dashed lines mark hydrogen bonds
1189 and the limits of the computational cell, respectively. The double arrows indicate
1190 interatomic distances in Å.
1191

Figure.6

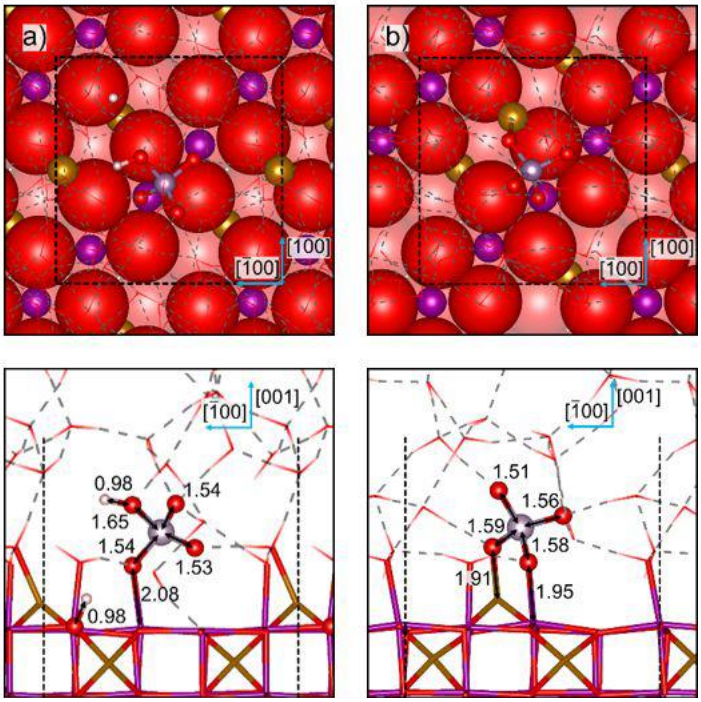

1192

1193 **FIGURE 6.** Top and side view of the aqueous inner-sphere species (a) HPO_4^{2-} and
1194 (b) PO_4^{3-} in acid and alkaline conditions, respectively. Tetrahedral Fe_A atoms are in
1195 orange, octahedral Fe_B atoms are in violet, O atoms are in red, P atoms are in blue
1196 and H atoms are in pink. Surface atoms are represented as (top panels) balls and
1197 (bottom panels) sticks, water solvent molecules are represented as wireframe and the
1198 solute molecules are represented as balls-and-sticks. Light and dark dashed lines
1199 mark hydrogen bonds and the limits of the computational cell, respectively. The
1200 double arrows indicate interatomic distances in Å.